PHOTONIC IMPLEMENTATION OF NEUROMORPHIC LEARNING AND SELF-ADAPTATION

by

RYAN ROBERT TOOLE

(Under the Direction of Mable P. Fok)

ABSTRACT

The field of neuromorphic engineering is focused on harnessing the advantages of neurobiological systems in any artificial systems that could stand to benefit from hybrid analog/digital processing techniques and the ability to learn and adapt. Here, a photonic system exemplifying a neuronal learning algorithm is developed, experimentally verified, and applied towards angle of arrival localization of microwave signals. Furthermore, a photonic Jamming Avoidance Response (JAR) device, mimicking the neurobiology of a genus of electric fish, is developed as a potential solution to spectral scarcity issues arising in wireless communications.

INDEX WORDS: Photonics, Neuromorphic engineering, Optical neural networks, Nonlinear optical signal processing, Radio frequency photonics, Localization, Spectral scarcity

PHOTONIC IMPLEMENTATION OF NEUROMORPHIC LEARNING AND SELF-ADAPTATION

by

RYAN ROBERT TOOLE

B.S., The University of Georgia, 2013

A Thesis Submitted to the Graduate Faculty of The University of Georgia in Partial Fulfillment of the Requirements for the Degree

MASTER OF SCIENCE

ATHENS, GEORGIA

2015

PHOTONIC IMPLEMENTATION OF NEUROMORPHIC LEARNING AND SELF-ADAPTATION

by

RYAN ROBERT TOOLE

Major Professor:	Mable P. Fok
Committee:	Peter Kner
	Caner Kazanci

Electronic Version Approved:

Suzanne Barbour
Dean of the Graduate School
The University of Georgia
August 2015

ACKNOWLEDGEMENTS

I would like to thank a number of people for help with this work, firstly Dr. Fok. I can't imagine working with another major professor, and the motivating and fun lab culture that she has developed in just two years has been crucial in the completion of my graduate obligations. The graduate students, Jia Ge, Qi Zhou, and Mary Locke, also played a major role, and their assistance over the years is greatly appreciated. Furthermore, the lab presence and consistent hard work of the undergraduate students, Alex, Aneek, and Nicole, were motivating factors in finalizing my thesis.

I'm grateful for both Dr. Kner and Dr. Kazanci participating in my studies as my committee members and, lastly, for Clodagh Miller's assistance with countless matters pertaining to registration and graduation. She continues to work closely with every graduate student and has played an important role in ensuring that the new college runs smoothly.

TABLE OF CONTENTS

Page

ACKNOWLEDGEMENTS iv

CHAPTER

1 INTRODUCTION 1

2 BIOLOGICAL SPIKE PROCESSING 5

The Leaky Integrate-And-Fire Neuron Model 5

Learning and Spike Timing Dependent Plasticity 7

3 PHOTONIC SPIKE PROCESSING 10

The Photonic Integration Parallel 10

The Photonic Neuron Model 11

4 EXISTING PHOTONIC NEUROMORPHIC CIRCUITS 17

Basics of Localization 17

The Crayfish Tail-flip Escape Response 18

Photonic Spike Timing Dependent Plasticity 22

Supervised Learning and Principle Component Analysis 25

5 A NEW SPIKE TIMING DEPENDENT PLASTICITY MODEL APPLIED TOWARDS ANGLE OF ARRIVAL DETECTION AND LOCALIZATION 28

Introduction 28

Photonic Implementation of Spike Timing Dependent Plasticity 29

Angle of Arrival Localization Based on Neuronal Learning Behavior 34

Conclusion 40

6 JAMMING AVOIDANCE RESPONSE 41

Introduction 41

Eigenmannia Jamming Avoidance Response Circuitry 43

Photonic Jamming Avoidance Response Circuitry 48

Conclusion 67

7 CONCLUSIONS 69

REFERENCES 71

APPENDICES 79

A JAR OPTISYSTEM SCREEN CAPTURE 79

B JAR P-UNIT OPTISYSTEM SCREEN CAPTURE 80

C JAR T-UNIT AND ELL OPTISYSTEM SCREEN CAPTURE 81

D JAR TS OPTISYSTEM SCREEN CAPTURE 82

E JAR MAJOR COMPONENT PARAMETERS 83

CHAPTER 1

INTRODUCTION

Today's powerful computers, complete with ever higher numbers of processor cores, expansive memory upgrades, and simply more approachable software development kits and interfaces, have facilitated the use of computationally intensive algorithms in nearly every facet of modern society. The pervasiveness of advanced computation has in turn expedited technological growth by altering the way in which scientists perform research, allowing for the modeling of systems previously too complex to simulate. The progression of advanced modeling and optimization techniques and effectively any technology utilizing computation is, quite obviously, affected by the advancement of signal processing capability. Consequently, better, faster computer technology is of perpetual interest, and, considering the physical limitations of traditional transistor-based processing, fields such as quantum computing and neuromorphic engineering are receiving attention due to their promise of improving processing capability directly and allowing for intelligent, automated signal processing, respectively.

The latter, neuromorphic engineering, is focused on mimicking neurobiological processing systems with electronics in an effort to harness any of the advantages neurobiological systems have over the computational mainstay. Despite their use of slow, stochastic processing methods, neurobiological systems are capable of outperforming the best of modern day supercomputers at complex tasks while drawing little power [1]. For example, the inner ear in cooperation with the brain is capable of detecting sound over a range of 120 decibels and filtering out undesirable sounds in a cacophonous environment, discerning individual inputs [2].

This rather incredible feat is far from achievable by any currently existing artificial system, and it's accomplished with the inner ear using just 14 microwatts [2].

The abilities of neural architectures to learn and adapt, changing their behavior with experience, and their parallel, inhomogeneous nature allow for the realization of such impressive acts [1]. As the human brain develops and the hundreds of billions of neurons are inundated with repetitive stimuli, specialization occurs as signal patterns are recognized, and sections of the neuronal structure are dedicated to particular subtasks [3]. This inhomogeneity allows for massively parallel processing, alleviating the need to waste energy in excessively transporting data, which in part explains the efficiency of biological circuitry [3].

Further contributing to the efficiency is the use of hybrid analog/digital components, as individual neurons work similar to analog-to-digital converters, recognizing input patterns, integrating these signals analogously, and outputting digital-like signals with high signal-to-noise ratios (SNR) [2]. This behavior serves to effectively regenerate a signal being transmitted throughout a neural network by integration and emission of a "clean" pulse at each neuron, while also allowing for asynchronous operation [3]. Ultimately, the analog properties of biological neurons allow for computational efficiency and asynchrony, and the digital properties allow for the implementation of complex computations by minimizing noise accumulation, which would otherwise threaten pure analog computation primarily in the form of thermal noise [2,4].

Lastly, the capabilities of neurobiological systems that set them furthest apart from artificial systems is learning and adaptation. Individual neurons within a network are connected to hundreds of other neurons by synapses, and these connections between each neuron can be modified in response to stimuli. The strength, or weight, of the connection between two neurons can be adjusted based on the relative timing of neuronal firing on either side of their synaptic

connection [5]. This process, known as spike timing dependent plasticity (STDP) can be summarized by the axiom, "neurons that fire together, wire together." Essentially, if a neuron's firing is casually connected to another neuron's firing over a period of time, those two neurons are more likely to fire together in the future [6]. STDP describes how neural networks are capable of developing into the inhomogeneous complexities observed in nature.

In the past, the nature of Moore's law, predicting that the number of transistors per square inch on integrated circuits has and seemingly will double every year, has undoubtedly drawn away interest in alternative processing methods, such as neuromorphic processing; however, Moore's prediction isn't entirely accurate and has shown signs of slowing [1]. As such, interest in neuromorphic engineering is growing and has manifested itself in a number of different research avenues. Physical chips have been designed which utilize feedback principles to adjust the synaptic weights of their artificial neurons, and massive neural networks with billions of neurons and trillions of connections have been simulated [3]. Every instance of neuromorphic research, despite the field's diverse nature, is invariably focused on both furthering our knowledge of neurobiological systems and searching for principles that can be applied to currently existing technologies [3]. New technologies like nanoscale transistors, memristors, quantum devices, and, the focus of this work, photonic circuits, are promising directions for research [1].

Neuromorphic signal processing alone, implemented electronically, aids in satiating the continuous interest in progressing processing potential, but the implementation of neuromorphic principles optically stands to improve upon modern processing capabilities even more dramatically. Photonics offers a number of advantages over electronics, which has led to the widespread integration of photonic circuitry in preexisting systems. For one, photonic systems

have incredibly large bandwidths, with standard communication optical fiber having an approximate bandwidth of 3 THz, which creates huge multiplexing potential. Also, photonic signal processing is credited with near-instantaneous response times, with integration times on the picosecond and even femtosecond timescale. Furthermore, optical fibers are notably lighter than radio frequency (RF) cables and boast considerably less loss, with just 0.2 dB/km loss in standard communication fiber. Lastly, the electromagnetic immunity of optical systems minimizes noise, resulting in more accurate and secure communications [7]. As such, the realization of neurobiological systems with photonic circuitry takes advantage of these described characteristics to achieve ultrafast processing at rates nearly billions of times faster than that of actual neural networks.

The motivation of this work is multi-pronged, involving the actualization of a photonic circuit that illustrates the fundamental, neuronal learning algorithm, STDP, and the development of both an STDP-inspired localization device and a jamming avoidance response (JAR) device based upon the neurobiology of a particular genus of fish known for utilization of electrolocation [8,9]. This comprehensive study highlights the viability of photonics in exemplifying fundamentals of neurobiology, while illustrating a prime motivation of all neuromorphic research, which is to uncover and apply neurobiological principles to existing technology or for any practical purpose.

CHAPTER 2

BIOLOGICAL SPIKE PROCESSING

The Leaky Integrate-and-Fire Neuron Model

Photonic neuromorphic engineering, while still surely in its infancy, has received attention primarily in the development of photonic neurons based upon a well-studied paradigm, the leaky integrate-and-fire (LIF) spiking neuron model. This biological computation abstraction describes how a neuron unit receives and integrates individually weighted and delayed electrical inputs over time and outputs spikes when the integrated response passes a certain threshold [10]. A single LIF neuron implements basic operations such as delaying, weighting, spatial summation, temporal integration and thresholding towards performing temporal logic and adaptive feedback [10]. The biological LIF neuron primarily consists of a dendritic tree, a soma, and an axon, as illustrated by Figure 2.1.

The dendritic tree serves to collect and sum the inputs, whether positively or negatively weighted (excitatory or inhibitory inputs), from other neurons, and the summation serves to alter the soma's state. The neuron receives N inputs, $\sigma_i(t)$, each representing conductance induced in a synapse. The inputs, continuous time series of analog spikes, each have a weight, w_i, whether positive or negative, and delay, δ_i, and are combined through pointwise summation, $\sum_{i=1}^{N} w_i \sigma_i(t - \delta_i)$. Acting as the integrator, the soma's state variable, $V_m(t)$, the voltage across the membrane, decreases in response to excitatory inputs and increases in response to inhibitory inputs. A series of inputs close in time or of particularly large amplitude affect the state variable more dramatically. The integral, $V_m(T) = V_{rest} - \frac{1}{C_m}\int_{-\infty}^{T} I(t) e^{-\frac{T-t}{\tau_m}} dt$, depicts the exponentially

weighted temporal integration of the input currents divided by the capacitance of the soma. Here, $t_m = R_m C_m$ is the integration time constant, R_m is the membrane resistance, C_m is the capacitance, and $I(t) = V_m(t) \sum_{i=1}^{N} w_i \sigma_i(t - \delta_i)$ is the current induced by the inputs. [10,11]

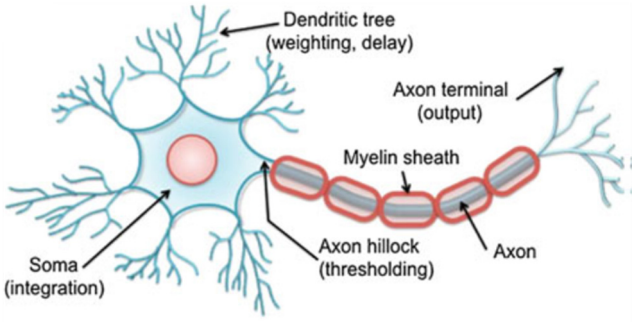

Figure 2.1. Biological LIF spiking neuron model, consisting of a dendritic tree, which collects and sums inputs from other neurons, a soma, which performs integration of the inputs, and an axon, through which the neuron outputs a spike when the voltage across the soma exceeds a certain threshold [10].

At the interface between the soma and the axon, thresholding occurs, and the neuron's output, $O(t)$, is decided. If the magnitude of the integrated signal drops below a particular threshold, V_{thresh}, then the neuron outputs a spike; thus, if $Vm(t) < Vthresh, O(t) = 1$. For a short period of time after emitting a spike, known as the refractory period, no other spike can be issued. So, if $O(t) = 1, O(t - \Delta t) = 0$, for Δt less than or equal to $T_{refract}$. Furthermore, $V_m(t)$ is reset to V_{rest}, its resting potential. The neuron's output, a continuous time series of spikes, is then transmitted from the axon to other neurons in the network. An individual LIF neuron's behavior is governed by the weights, w_i, the delays, δ_i, its native threshold V_{thresh}, resting potential V_{rest}, its refractory period $T_{refraft}$, time varying conductance changes $\sigma(t)$, and its

integration time constant τ_m. The effects of these variables on $V_m(t)$ can be concisely explained by the differential equation:

$$\frac{dV_m(t)}{dt} = \frac{V_{rest}}{\tau_m} - \frac{V_m(t)}{\tau_m} - \frac{1}{C_m} V_m(t)\sigma(t)$$

This equation indicates three major influences on $V_m(t)$: active pumping, passive leakage of current, and external inputs which generate conductance changes in the membrane. [11]

The LIF is the staple neuromorphic primitive that has proven itself computationally powerful for a number of reasons. For one, LIF integration exemplifies basic temporal summation necessary for a plurality of inputs, and its thresholding serves to reduce dimensionality of incoming info and clean up any amplitude noise. The refractory period and reset condition clean up timing jitter, prevent excessive temporal spreading of excitatory activity, and place a bandwidth cap on output of a unit. The neuron's ability to spontaneously generate pulses ensures that information propagating through a system is not eventually lost to noise and allows for spiking independent of inputs. Lastly, the LIF model is capable of implementing learning algorithms and emulating adaptability in response to environmental and system conditions.

Learning and Spike Timing Dependent Plasticity

The LIF model's potential for adaptability allows for massive LIF-based networks to exhibit the reconfigurable characteristic displayed by biological neural networks. Adaptability rules are essential for the stability of large-scale systems and ensure that systems are capable of operation despite unit parameter inconsistencies or even the total failure of an individual unit. The ability for neurobiological architectures to learn and adapt, if properly mimicked, could allow for artificial systems to adapt to environments that are either too complex to characterize or for which a priori knowledge is not readily available. Neuromorphic engineers have

successfully developed circuits capable of exhibiting synaptic modification, enabling devices to change their behavior with experience and also to overcome device parameter variability inherent to manufactured technologies [1].

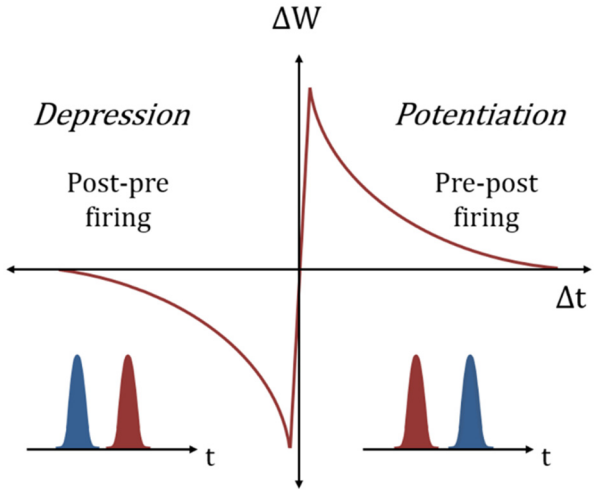

Figure 2.2. Illustration of the STDP algorithm. The red pulse is the presynaptic spike, and the blue pulse is the postsynaptic spike. Both depression and potentiation of the synapse is possible depending on the timing of the spikes.

The algorithm responsible for learning, spike timing dependent plasticity (STDP), is based on the relative timing of a neuron's inputs (presynaptic spikes) and outputs (postsynaptic spikes). The timing of these pre- and postsynaptic spikes compared at each neural interconnect, ultimately determines whether the strength of the synaptic connection between a pair of neurons is strengthened or weakened and is described by two possible scenarios, pre-post firing and post-pre firing. For pre-post firing the synapse is strengthened, as the presynaptic spike is assumed to have contributed to the firing of the postsynaptic spike in a process called "potentiation." In post-pre firing "depression" occurs as the postsynaptic spike is fired prior to the neuron receiving a

presynaptic spike, and the synaptic connection is weakened. The change in weight, as determined by the relative timing of pre- and postsynaptic spikes is depicted by Figure 2.2, where $\Delta t = t_{post} - t_{pre}$, t_{post} is the time at which a neuron fires, and t_{pre} is the time at which it receives an input. STDP is just one of the many Hebbian learning rules explored by neuromorphic engineers, which all propose a means of modeling synaptic plasticity. However, considering the sharp discontinuity at $\Delta t = 0$, STDP is most properly implemented on the ultrafast time scales exhibited by photonic systems [10].

STDP emphasizes connections between neurons causally related in a decision tree, and the connections along which a powerful signal travels tend to strengthen. Strengthening causally related signals, the algorithm serves to minimize information difference between the input and output channels of an individual neuron. STDP operates on each neural connection, making it suitable for massive, parallel networks, and its simplicity allows for different learning tasks, such as unsupervised and supervised learning. For unsupervised learning, automatic adjustments are made to the synaptic connections within a network based on overall signal statistics, and, for supervised learning, a system undergoes changes as a result of being compared to a teacher, which exhibits some desirable behavior. STDP-based supervised learning has already been implemented in a photonic system demonstrating adaptive feedback, and the algorithm shows promise in being used towards applications such as sensory processing, autonomous robotics, principle component analysis (PCA), and independent component analysis (ICA) [10,12,18,19].

CHAPTER 3

PHOTONIC SPIKE PROCESSING

The Photonic Integration Parallel

The LIF neuron is the most widely accepted model for an individual processing unit within neuromorphic systems for its simplicity, ability to incorporate scalable learning algorithms, and its suitability for implementation in inhomogeneous, parallel networks. As such, demonstration of the LIF spiking behavior with optical components was an important step towards enabling neuromorphic processing at rates millions of times faster than that of biology, while promising to expand upon optical processing capabilities and to open up a new avenue of neuromorphic research. Fascinatingly, there exists a parallel between the differential equation governing the membrane potential in the LIF model and the equation governing the gain dynamics of the widely used semiconductor optical amplifier (SOA), which uses a semiconductor gain medium and operates similarly to a laser diode with the end mirrors replaced with anti-reflection coatings. The typical single-mode waveguide has overlap in the active region of the semiconductor, which is pumped with electric current, creating a carrier density in the conduction band. Input optical signals are then capable of inducing optical transitions, i.e. stimulated emission, from the conduction band to the valence band [7]. The gain dynamics of the device are described by the top equation, with the membrane voltage equation for reference:

$$\frac{dN'(t)}{dt} = \frac{N'_{rest}}{\tau_e} - \frac{N'(t)}{\tau_e} - \frac{\Gamma a}{E_p} N'(t) I(t)$$

$$\frac{dV_m(t)}{dt} = \frac{V_{rest}}{\tau_m} - \frac{V_m(t)}{\tau_m} - \frac{1}{C_m} V_m(t) \sigma(t)$$

where $N'(t) = N(t) - N_0$ is the primary state variable, which represents the carrier density above transparency, with $N(t)$ being the actual carrier density and N_0 being the density at transparency. τ_e is the carrier lifetime, N'_{rest} is the resting carrier density when subjected to pumping, and $I(t)$ is the input light intensity. The mode confinement factor Γ and differential gain coefficient *a* are native constants of the SOA, and E_p is the photon energy. [10,11]

Just as the membrane voltage in the LIF spiking model is affected by active pumping, passive leakage, and external inputs, so too is the carrier density above transparency for the SOA. Here, active pumping in the form of applied driving current to the SOA defines a resting carrier density in the absence of external inputs, leakage occurs in the form of spontaneous emission, leading to carrier decay, and external inputs result in stimulated light emission, serving to discharge the device, rapidly depleting the carrier density. Evidently, the membrane voltage model and the SOA gain dynamics model are nearly identical; however the two equations operate on drastically different timescales. The integration time constant in the biological neuron equation is typically around 10 ms, and τ_e in the SOA equation can be as low as 10 ps [10,11]. Consequently, photonic neurons implementing this integration technique could be hundreds of millions of times faster than their biological predecessors.

The Photonic Neuron Model

The first photonic neuron, exhibiting both integration and thresholding, was developed in 2009 and expanded upon in the ensuing years [4,11,13]. The optical implementation, depicted in Figure 3.1, consists of N optical inputs, each with a variable attenuator and variable delay line, coupled together with a sampling pulse train, an integrator stage consisting of an SOA and an optical bandpass filter, and a thresholding stage consisting of a nonlinear-fiber-based optical loop mirror filter. The optical spikes, with approximate 3 ps pulsewidths, were generated by means of

a mode-locked laser at a repetition rate of 1.25 GHz, and Mach-Zehnder modulators (MZMs) and bit error rate testers were employed to create different pulse patterns with various delays and weights.

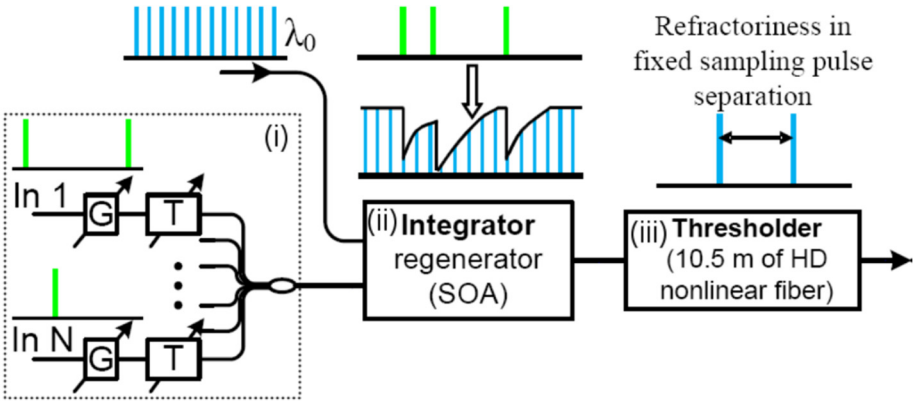

Figure 3.1. First photonic neuron, exhibiting the fundamental processes of the LIF spiking model. (i) shows the dendritic tree accepting multiple inputs at various weights and delays. (ii) illustrates integration as performed by an SOA. (iii) illustrates thresholding as performed by a nonlinear optical loop mirror [13].

The sampling pulse train, a low power series of pulses at a wavelength of λ_0, different than that of the neuron inputs, is used to sample the SOA gain. Considering the low power of the sampling pulses, the pulses' effect on the SOA gain is negligible when compared to that of the input signal; thus, the amplification of the sampling pulse train provides a measurement of the SOA carrier density, as affected by the input signal. A bandpass filter after the SOA passes the sampling pulses, and Figure 3.2 compares the consequent sampled SOA gain dynamics (Figure 3.2(a)) to the input pulse train (Figure 3.2(b)). As is evident, the sampling pulses are amplified to a lesser extent when aligned in time with the input pulses, displaying the nonlinear optical effect of cross-gain modulation (XGM). Basically, the high power input signal depletes the SOA gain,

resulting in the minimized amplification of the sampling pulses. Figure 3.2 illustrates the nature of gain recovery in an SOA. Due to the high temporal clustering of pulses from 0 to 600 ps, the gain remains suppressed, but, as can be seen past the 600 ps mark, the gain has more time to recover between inputs.

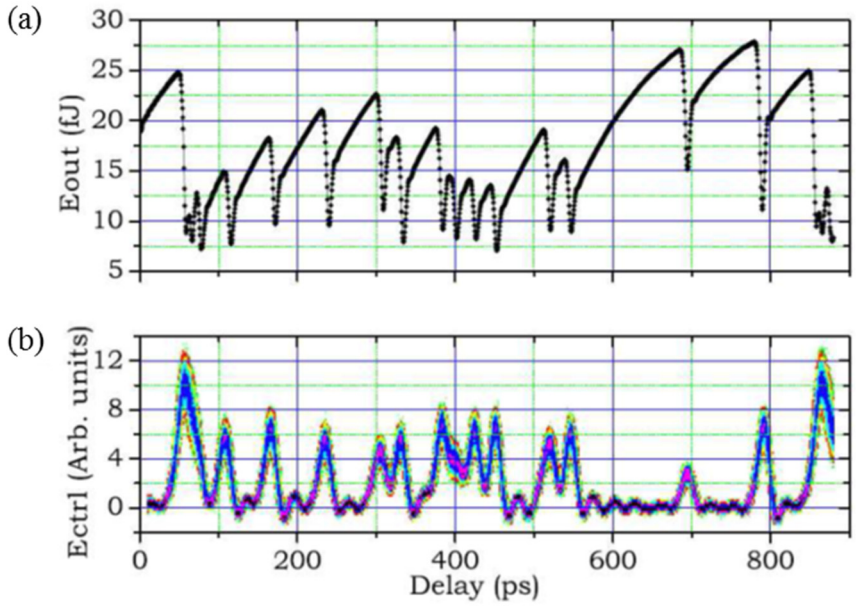

Figure 3.2. Comparison of the output of the integrator and its input. (a) The output illustrates the carrier density of the SOA at various times. (b) The optical input pulses are at various delays and weights [13].

The integrator output is then sent to the thresholder unit, based upon a nonlinear optical loop mirror (NOLM), which takes advantage of the intensity-dependent phase shift induced in highly nonlinear fiber to suppress spikes below a certain threshold [14]. In an ordinary loop mirror, the entirety of the optical input is reflected back down its input path. This is due to the 90º phase shift experienced by the counter-propagating signal at each pass through the coupler, which results in total destructive interference in one branch and constructive interference at the

input port. The NOLM structure includes a 90/10 coupler and a length of highly nonlinear fiber, giving rise to nonlinear effects, e.g. doubling input intensity doesn't necessarily result in twice the output intensity. Consequently, signals with high enough intensity experience a phase shift such that the destructive interference at the output port is no longer experienced; however, signals below a certain threshold experience a negligible phase shift in the fiber and still destructively interfere at the output port [14]. A recently developed device, the dual resonator enhanced asymmetric Mach-Zehnder interferometer, more succinctly referred to as the DREAM, could exceed the NOLM in thresholding performance, and its transfer function, indicating a sigmoidal response for output energy with respect to input energy, is shown in Figure 3.3 to illustrate the concept of thresholding [10].

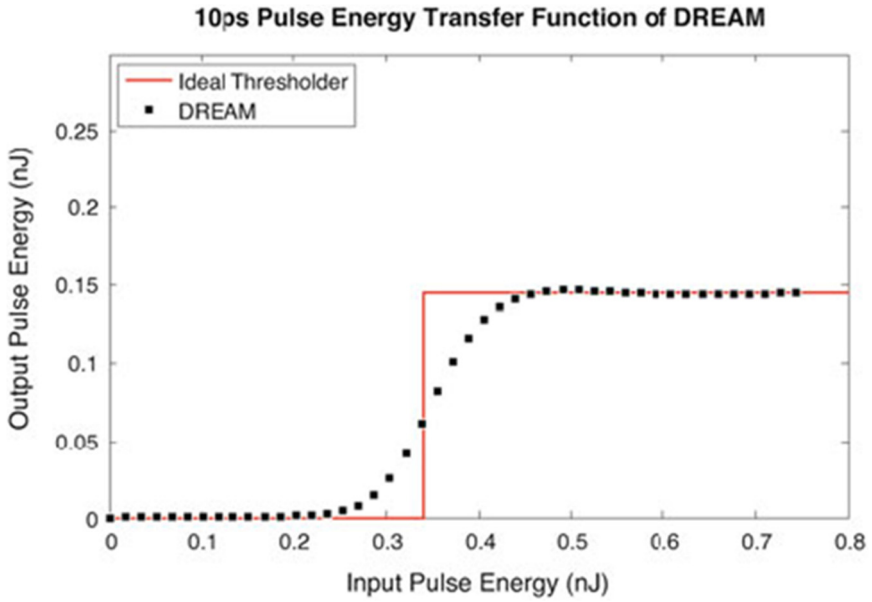

Figure 3.3. Simulated thresholding capabilities of the DREAM, a device operating similar in principle to the NOLM. The black square points indicate the simulation results and an ideal thresholding response, a Heaviside step function, is shown in red. For this simulation, a 350 pJ threshold level is indicated for 10 ps input pulses [10].

The NOLM-based thresholder suppresses the sampling pulses at times when inputs resulted in the carrier density dropping below a certain threshold and allows pulses above the threshold to pass, which is inverted behavior with respect to the standard behavior of the LIF model. Later photonic neuron designs included an optical inverter and yet another thresholder to produce the ideal LIF response, as shown in Figure 3.4. [11]

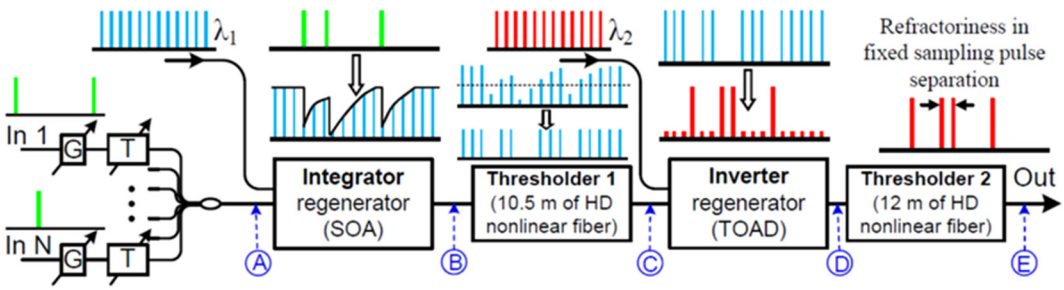

Figure 3.4. Improved photonic LIF neuron, consisting of N inputs, an integrator, two thresholders, and a TOAD-based inverter. The signal at (A) is the weighted and delayed neuron input, (B) is the integrated response, (C) is the inverted thresholded LIF output, (D) is the non-inverted TOAD output, (E) is the thresholded, final, correct, LIF response [11].

The inverter is based on the conventional terahertz optical asymmetric demultiplexer (TOAD), which is essentially a modified NOLM [15]. The inverted output from the first thresholder acts as the control signal, which serves to induce a phase shift in another set of sampling pulses injected into the TOAD loop. Ultimately, the sampling pulses output through the reflection port of the TOAD are inverted with respect to the control signal, but further thresholding is necessary as the inversion is not ideal [11]. The signal at point E, depicted in Figure 3.4, is the desirable LIF response. This photonic model successfully demonstrates means

of ultrafast integration and thresholding, but is without a reset condition or adaptive circuitry, fails to generate optical pulses, and, considering the reliance on sampling pulse trains at a fixed repetition rate, doesn't exhibit asynchronous behavior. Since the development of this original system, some efforts have been made towards developing photonic neurons that better represent the LIF model, such as the development of an asynchronous model based on the nonlinear effect of four wave mixing (FWM) [16], but the original bench model successfully demonstrated ultrafast cognitive computing and inspired the development of a number of practical computing and signal processing applications [10].

CHAPTER 4

EXISTING PHOTONIC NEUROMORPHIC CIRCUITS

Several small-scale neuromorphic circuits have been developed based on the photonic LIF neuron previously described, such as an auditory localization circuit inspired by the barn owl, with possible light detection and ranging (LIDAR) localization applications [10], a circuit mimicking the tail-flip escape response of crayfish [17], which demonstrations ultrafast pattern recognition, and principle and independent component analysis systems, useful for reduction of dimensionality in complex, multidimensional signals [18,19]. The simple circuits that have been developed mimic important aspects of neuronal behavior, while providing the ultrafast speeds and low-latency typical of photonics.

Basics of Localization

The barn owl auditory localization algorithm illustrates the possibility of configuring a neuron to respond to sensory data from objects in a particular location, based solely on the basic integration and thresholding processes portrayed by the photonic LIF neuron. Figure 4.1(a) drawn from [10] shows the time difference of signals received from objects 1 and 2 at the owl's two sensors. The time differences observed by the owl for object 1 and object 2 are $\Delta T_1 = (t_{1a} - t_{1b})$ and $\Delta T_2 = (t_{2a} - t_{2b})$, respectively, and integration and thresholding behavior are depicted in Figure 4.1(b) and 4.1(c). For spikes sufficiently spaced out, e.g. the spikes received from object 1, the stimulated neuron response doesn't dip below a threshold, so the circuit fails to emit a spike; however, the spikes received by the sensors from object 2 are closer in time, preventing the neuron's SOA carrier density from recovering and resulting in the neuron

response dropping below the threshold. As such, the neuron emits a spike. The proof-of-concept was illustrated with the original photonic neuron model without signal inversion and additional thresholding. So, the basic neuromorphic circuit's spiking behavior is inverted.

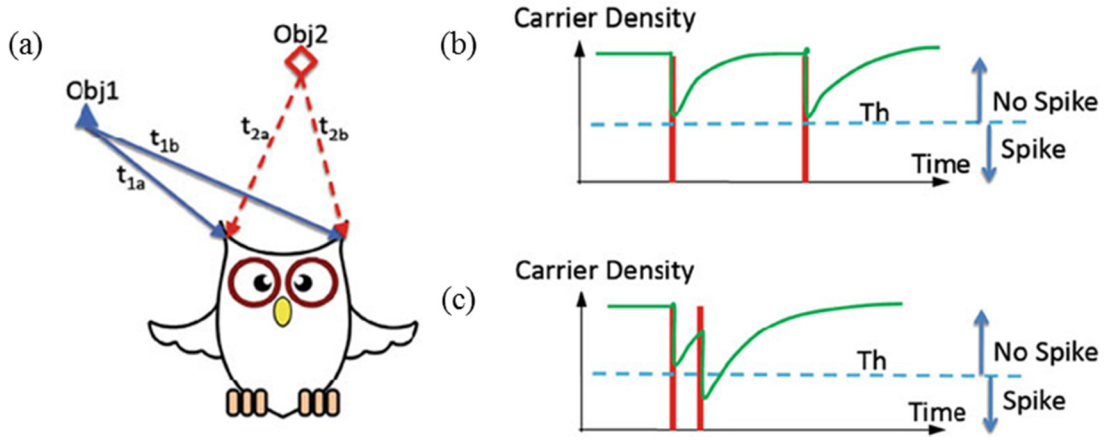

Figure 4.1. Barn owl auditory localization parallel [9]. (a) Depiction of time delays between the barn owls different sensors for signals arriving at different angles. (b) Integration and thresholding behavior of neural circuitry for sensing object 1. (c) Integration and thresholding behavior of neural circuitry for sensing object 2 [10].

The Crayfish Tail-flip Escape Response

The crayfish tail-flip escape response, as developed in [17], demonstrates a larger scale photonic neuromorphic model based on a life-or-death response of the crayfish, which relies on an accurate, fast neural response to specific stimuli. The developed device makes use of two electro-absorption modulators (EAM) for integration purposes and the previously described NOLM thresholders to respond exclusively to certain spike patterns. Operating on picosecond time scales, the accurate response of the processor shows potential for being applied in defense applications for which critical decisions, made faster than possible by humans or electronics,

could save lives. One possible application is a circuit used to determine pilot ejection from military aircraft.

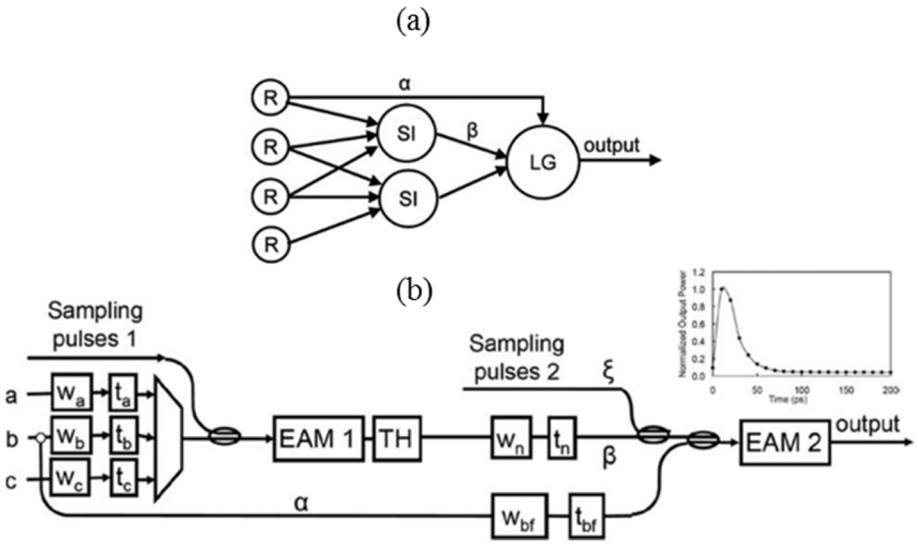

Figure 4.2. (a) Illustration of the crayfish tail-flip escape response, with receptors (R), sensory inputs (SI), the lateral giant (LG), and time delays, α and β. (b) Illustration of the optical implementation of the escape response, with three inputs, a, b, and c, weights (w), delays (t), electro-absorption modulators (EAM), and a thresholder (TH). The inset displays the recovery profile of cross-absorption modulation in an EAM [17].

In the basic crayfish tail-flip neural model, as shown in Figure 4.2(a), spike signals are received at receptors, R, and transmitted to a set of neurons, entitled sensory inputs, SI. Each SI is set to respond to a particular pattern of spikes from the input receptors. The spikes emitted from the SI are launched to the lateral giant (LG) alongside a signal from one of the receptors, where further integration is performed. The LG responds only when the integrated signals are close temporally and of high enough power. The optical analog explored in [17] and illustrated by Figure 4.2(b) consists primarily of three input spikes, a, b, and c, at various weights and

delays, an EAM and optical thresholder serving as a parallel to the SI, and a second EAM serving as the LG.

An EAM is a semiconductor device that exhibits behavior opposite to that of the SOA, serving to absorb photons from an optical input [20]. In this circuit, a sampling train of pulses is launched into the EAM alongside the three receptor inputs. In a display of cross-absorption modulation (XAM), the sampling pulses are able to pass through the device only when temporally aligned with high-power control pulses, which exhaust the EAM's absorption potential. The nonlinear optical effect utilized for integration, XAM, can be seen in the EAM transmittance subsections of Figure 4.3. The first EAM and thresholder outputs in response to different inputs are displayed in Figures 4.3(i) through 4.3(vi), exhibiting the XAM effect. Figures 4.3(v) through 4.3(xiii) show the inputs and outputs of the setup's second EAM, serving as the LG, when the device is configured to detect different signal patterns. Ultimately, the researchers were able to develop and configure a photonic system to respond only to a specific set of inputs and in a particular integration window determined by the recovery time of the EAM. The work presents yet another means of performing integration with a photonic device towards developing an ultrafast processing device inspired by neural circuitry.

Figure 4.3. Illustration of different pattern recognition configurations. (i)-(iv) First integrator and thresholder inputs and outputs. (v)-(vii) Second neuron's inputs and outputs when set to detect patterns "abc" and "ab-." (viii)-(x) Second neuron's inputs and outputs when set to detect only "abc." (xi)-(xiii) Second neuron's inputs and outputs when no patterns are detected [17].

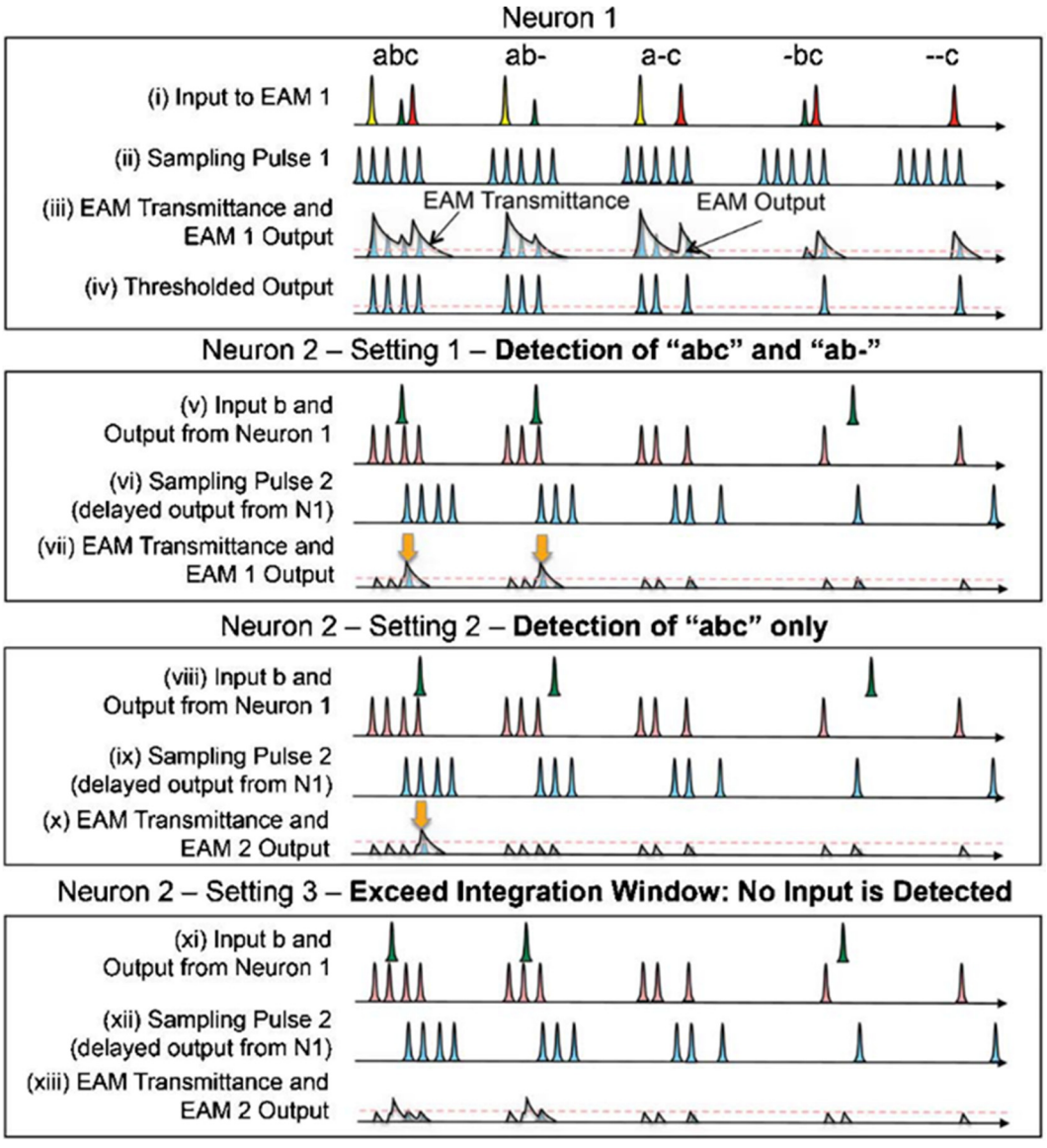

Photonic Spike Timing Dependent Plasticity

One the most important neural imitations to be explored with photonic neuromorphic engineering is learning and adaptation. The spike timing dependent plasticity (STDP) algorithm has been applied, non-optically, to control systems and for adaptive feedback applications, including coincidence detection, sequence learning, navigation path learning, and directional selectivity in regards to visual response [21-27]. The STDP behavior has been used in applications-based contexts and also as the general learning rule in systems exemplifying cognitive computing capabilities. In said systems the rule serves as the operating principle for information-theoretic algorithms like mutual information maximization, information bottleneck optimization, and independent component analysis [12].

In a recent work by Fok et al., the general STDP response was experimentally achieved and applied in a photonic example of supervised learning, where a spike processing unit learned to replicate a particular spiking pattern as instructed by a teacher signal [12]. The SOA and EAM's complimentary effects of XGM and XAM were used to generate the STDP curve in response to two ultrashort optical pulse inputs, one serving as the presynaptic spike and the other as the postsynaptic spike. Figure 4.4(a) shows the experimental setup, depicting the unequal split of power between each branch, such that a larger portion of the postsynaptic spike is sent to the SOA and a larger portion of the presynaptic spike is sent to the EAM. The relative time delay between the pre- and postsynaptic spikes entering the system is controlled by a variable delay line, an optical bandpass filter in the SOA branch passes the presynaptic spike, and another optical bandpass filter in the EAM branch passes the postsynaptic spike.

To construct the depression window, the delay is adjusted such that the postsynaptic spike precedes the presynaptic spike, resulting in the trailing pulse experiencing lesser

amplification in the SOA branch due to the gain depletion induced by the leading pulse. When the delay is near zero, the SOA has little time to recover, and minimal amplification of the passed presynaptic spike is observed. For larger time differences between the two pulses, the SOA is able to recover further after the leading postsynaptic spike, so the presynaptic spike experiences further amplification (shown in Figure 4.4(b-iii), region I). In the EAM branch, the passed postsynaptic spike is similarly leading and therefore experiences an identical response for all negative values of $\Delta t = t_{post} - t_{pre}$, where t_{pre} and t_{post} are the timing of the pre- and postsynaptic spikes, respectively (shown in Figure 4.4(c-iii), region III).

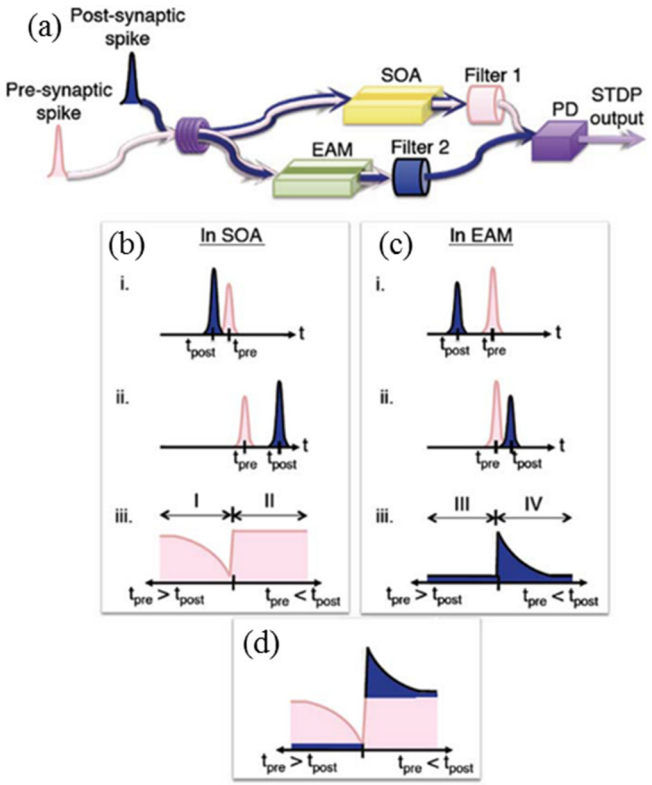

Figure 4.4. (a) Optical STDP based on an EAM and SOA. (b) Formation of the depression window, primarily described by the SOA. (c) Formation of the potentiation window, primarily described by the EAM. (d) Linear combination of the SOA and EAM outputs [12].

To construct the potentiation window, the delay is then adjusted so that the presynaptic spike precedes the postsynaptic spike. In this scenario for all positive Δt, the leading pulse experiences the same level of amplification in the SOA branch, as illustrated by Figure 4.4(b-iii) in region II. Figure 4.4(c-iii) shows the XAM response of the EAM in region IV as the positive Δt is varied. The leading pulse induces absorption saturation in the device, and for small Δt the trailing postsynaptic pulse experiences nearly no absorption; however, for larger delays the EAM has more time to recover and the trailing pulse is further diminished. When the outputs of each branch are combined and the power is monitored over a range of negative and positive Δt values, the STDP curve can be reconstructed (Figure 4.4(c)), as shown by the results depicted in Figure 4.5. Different neurobiological systems often have different STDP responses with asymmetric potentiation and depression windows, so the researchers demonstrated their ability to tune their circuit's response by changing semiconductor device parameters and input pulse powers.

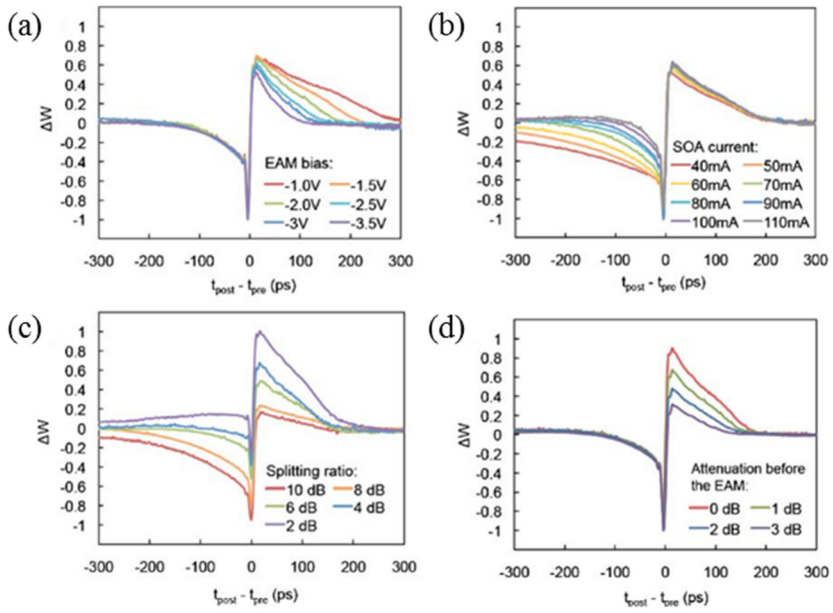

Figure 4.5. Reconfigurable STDP response. (a) Different EAM bias voltage. (b) Different SOA driving current. (c) Different spike splitting ratios. (d) Different input power to EAM [12].

Supervised Learning and Principle Component Analysis

To demonstrate supervised learning, this STDP circuit was employed in a setup similar to the one shown in Figure 4.6, which uses automatic gain control to adjust the output of a photonic pulse processor, effectively a photonic LIF neuron, in response to a teacher signal. In the proposed system, a teacher signal, which represents the spike pattern desired from the pulse processor, serves as the presynaptic signal, and the processor's output serves as the postsynaptic signal. Thus, the supervised learning system differs from the unsupervised learning system shown by Figure 4.6 as the presynaptic input is actually a fixed external signal. Ultimately, the two spike patterns are compared within the STDP system, and the device's output adjusts the weight of the processor input if the device is spiking in a manner different from that of the teacher signal.

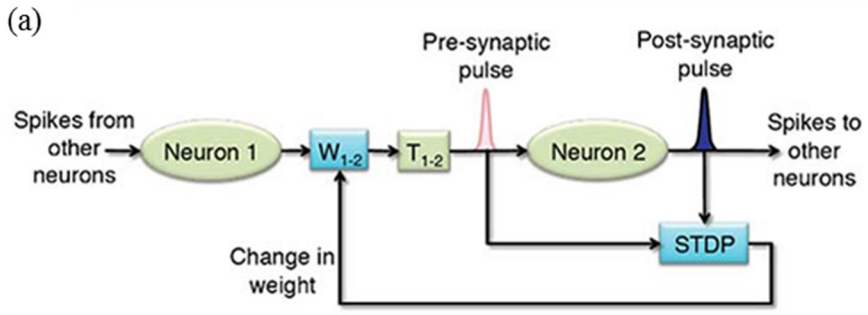

Figure 4.6. Schematic illustrating how a photonic STDP circuit could be implemented in a learning setting. This particular setup illustrates unsupervised learning [12].

The process is illustrated by Figure 4.7. Evidently, when the teacher input power is too low, voltage supplied to an electro-optic modulator (EOM), which works as an ultrafast tunable optical attenuator, is adjusted so that the input power is increased. If the input power is too high, the EOM driving voltage is decreased, lessening the teacher's power. Ultimately, the processor's

output directly mirrors its teacher input, and the experiment illustrates the potential for STDP being implemented in any system that may make use of automatic gain control. Furthermore, this work served as the first photonic representation of the STDP algorithm, serving as a major milestone in the progression of photonic cognitive signal processing.

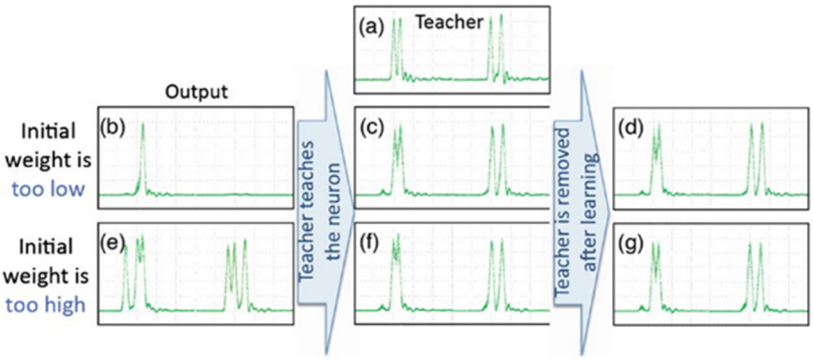

Figure 4.7. Experimental results for an automatic gain control device based on STDP. (a) Teacher input, indicating the desired pulse-processor response. (b)-(d) The initial power of the teacher input was too low, and gain is automatically adjusted accordingly. (e)-(g) The initial power of the teacher input was too high, and gain is automatically adjusted [12].

Various learning algorithms have been implemented in photonic applications by means of electronics, and the photonic STDP circuitry could replace the electrical elements of these systems. Recently, researchers have developed a photonic system capable of performing principle component analysis (PCA) on a set of wavelength-division multiplexed (WDM) inputs [18]. WDM is simply the combination of multiple signals at different wavelengths onto a single transmission line and is essential for large-scale photonic neural networks in which an individual processing unit receives inputs from a number of different units. In [18], a Hebbian learning rule is applied iteratively using electronics to perform PCA, which reduces the dimensionality of the

multivariate data by interpreting it relative to an eigenvector of the high-dimension space along the direction of maximum variance [10]. PCA is a means of interpreting data without a priori knowledge and is therefore ubiquitous in machine learning and computational neuroscience [10,18,28]. As such, WDM systems demonstrating PCA will subsequently be developed with photonic learning algorithms.

CHAPTER 5

A NEW SPIKE TIMING DEPENDENT PLASTICITY MODEL APPLIED TOWARDS ANGLE OF ARRIVAL DETECTION AND LOCALIZATION

Introduction

One of the primary efforts of this thesis is to simplify the photonic spike timing dependent plasticity (STDP) circuitry described in Chapter 4. Simplification of the system improves the scalability and reduces fabrication challenges, and fewer optical paths result in higher operation stability. In this chapter, a recently developed STDP system is described and experimentally verified. The proposed device makes use of the nonlinear optical effects of nonlinear polarization rotation (NPR) and cross gain modulation (XGM), in a single semiconductor optical amplifier (SOA), simplifying previous approaches towards generating an STDP response. Furthermore, one of the motivations behind pursuing neuromorphic engineering is the potential for recognizing practical applications for the explored neural processes.

As such, the following work is drawn from an Optics Express publication by Ryan Toole and Mable P. Fok entitled, "A photonic implementation of a neuronal algorithm applicable towards angle of arrival detection and localization [9]," in which we explore a photonic approach towards angle of arrival (AOA) measurement and localization of a microwave signal implementing the presented STDP circuitry. The STDP behavior has a unique capability of determining the angle as well as the direction of arrival, and AOA measurement is a powerful tool implemented in wireless localization schemes, capable of locating a microwave transmission source in three dimensions with only three measuring units [29]. In general, an AOA unit

consists primarily of an antenna array, measuring the time difference of arrival (TDOA) of an incident signal to determine the angle from which the signal arrived. AOA techniques based on ultrasound signals, RF signals, and ultra wideband (UWB) pulses have all been explored [29-35]. Localization schemes making cooperative use of various positioning techniques, such as AOA with time of arrival (TOA) and received signal strength (RSS) with TOA have also been explored [29,36,37]. Certain systems have proven capable of localization accuracies on the order of tens of centimeters, such as Hewlett Packard's smartLOCUS, utilizing an RSS and ultrasound technique, and the Ubisense and Sapphire Dart systems, both implementing UWB TDOA techniques; however, such accuracies generally require a highly complex and expensive system [29,33-35]. In recent years, a photonic AOA system was also proven powerful, yielding high accuracies, but the promising field of photonic microwave localization remains largely underdeveloped or unexplored [38]. Here, an STDP-based AOA measuring unit is simulated, and its accuracy and limitations are explored. Based on this AOA unit, a microwave transmitter localization scheme is then theoretically developed. The technique presented exhibits promise in multiple scenarios, for both use in an indoor and outdoor positioning system, depending on certain system parameters such as the spacing of the measuring units. Depending on the scale of the system, transmitters operating over a wide microwave frequency range can be located with centimeter accuracy at indoor distances of tens of meters, rivaling preexisting UWB approaches with approximately 20 cm accuracy [29].

Photonic Implementation of Spike Timing Dependent Plasticity

The desirable STDP response and the optical experimental setup for realizing it are shown in Figure 5.1. The STDP circuit is a relatively simple system that mainly consists of a single semiconductor optical amplifier (SOA), two bandpass filters, and a polarization beam

splitter (PBS). A polarizer and polarization controllers (PCs) are used for initial polarization alignment before operation. To experimentally verify generation of the STDP characteristic, two optical pulses at different wavelengths are generated using a fiber laser and four-wave mixing (FWM) and sent through the STDP circuitry at various time delays [8]. The pre- and postsynaptic (red and dashed blue, respectively) optical spike trains, at 1550.12 nm (λpre) and 1553.33 nm (λpost), respectively, maintain a repetition rate of 625 MHz at an average power of -4 dBm. Both spikes enter into the STDP circuit in the same polarization state, and a 600 ps variable optical delay line is inserted into the presynaptic branch to implement tunable time delay between the spikes.

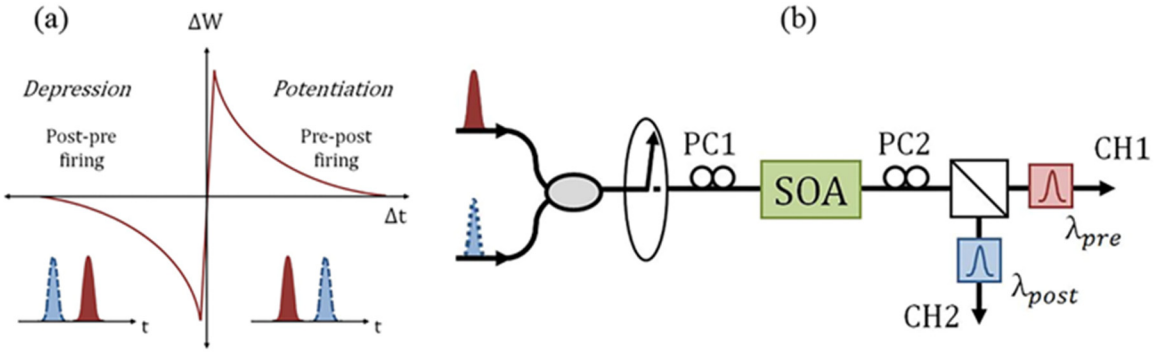

Figure 5.1. (a) Theoretical STDP curve. (b) STDP experimental setup - Oval with arrow: polarizer; PC1 and PC2: polarization controllers; SOA: semiconductor optical amplifier; Square with diagonal: polarization beam splitter; Colored squares: bandpass filters at λpre and λpost.

The delay is initialized such that the postsynaptic spike precedes the presynaptic spike by over 300 ps, and PC1, as labeled in Figure 5.1(b), is adjusted so that the input pulses experience the highest possible, equivalent gain at maximum separation. At a time difference of 300 ps, with t_{post} being significantly less than t_{pre}, the SOA has adequate time to recover between inputs, and each pulse experiences the same level of amplification and the same minimal polarization

rotation, allowing for PC2 to be properly initialized. This PC is adjusted so that the SOA output is initially aligned to one channel of the PBS, channel 1 (CH1), minimizing the throughput of channel 2 (CH2). Next, the delay is adjusted so that $\Delta t = t_{post} - t_{pre}$ ranges from 300 to -300 ps, and the output power of both channels is combined and measured at different delays to construct the STDP curve.

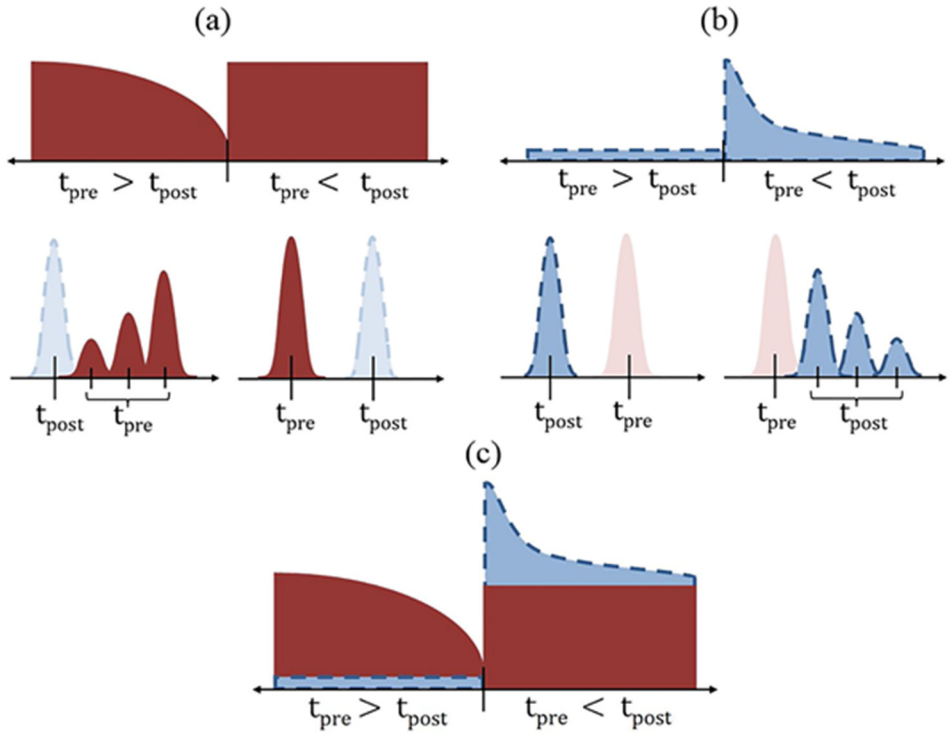

Fig. 5.2. (a) Photonic STDP channel 1 output. (b) Channel 2 output. (c) Channels 1 and 2 combined.

Figure 5.2 illustrates the means through which the depression and potentiation windows of the STDP response are generated. As shown by Figure 5.2(a), a gain depletion response of CH1 at the λ_{pre} wavelength is responsible for acquisition of the depression window. When a pulse enters the SOA and depletes the device's gain, the trailing pulse experiences minimal

amplification. For Δt values below zero, corresponding to the left side of Figure 5.2(a), the postsynaptic spike (dashed blue) precedes the presynaptic spike (solid red), and, if the time difference is small, the SOA has little time to recover. Consequently, the presynaptic spike experiences almost no amplification. As Δt becomes more negative, the spacing increases, and the SOA has more time to recover. This allows for the presynaptic spike to experience higher levels of amplification and results in the generation of the depression window, seen on the left side of Figure 5.2(a). If Δt is greater than zero, the leading presynaptic spike experiences the same maximum level of amplification across the entire range of positive Δt values and experiences no XGM, resulting in the right side of Figure 5.2(a).

As illustrated by the left side of Figure 5.2(b), for all negative Δt values, the preceding postsynaptic spike experiences no NPR, and the CH2 output at λ_{post} remains constant. When the postsynaptic spike follows shortly behind the presynaptic spike, however, the trailing spike experiences NPR due to the birefringence change in the SOA induced by the presynaptic spike. The effect is strongest for small Δt and decreases as Δt increases; thus, the right side of Figure 5.2(b) is realized. As indicated by Figure 5.2(c), the linearly combined power outputs of channels 1 and 2 for all values of Δt between -300 and 300 ps generate the STDP curve.

Prior to the full realization of the photonic STDP curve, the cooperative effects of XGM and NPR were exhibited in a simple experiment with a 1540.6 nm pulse pump and a 1550.12 nm CW probe. In the same polarization state, the CW signal and the pulse train, with 10 ps pulse widths and a 625 MHz repetition rate, were sent through an SOA and a PBS, with a 1550.12 nm bandpass filter and photodetector (PD) in each branch. Both XGM and NPR effects happen simultaneously in the SOA and the results are observed at each of the outputs of the PBS, CH1 and CH2, respectively. The resulting oscilloscope traces of both branches of the PBS are shown

in Figure 5.3(a). The XGM and NPR effects are exhibited by the green curve (bottom) and yellow curve (top), respectively, illustrating the feasibility of obtaining both STDP windows with a single SOA.

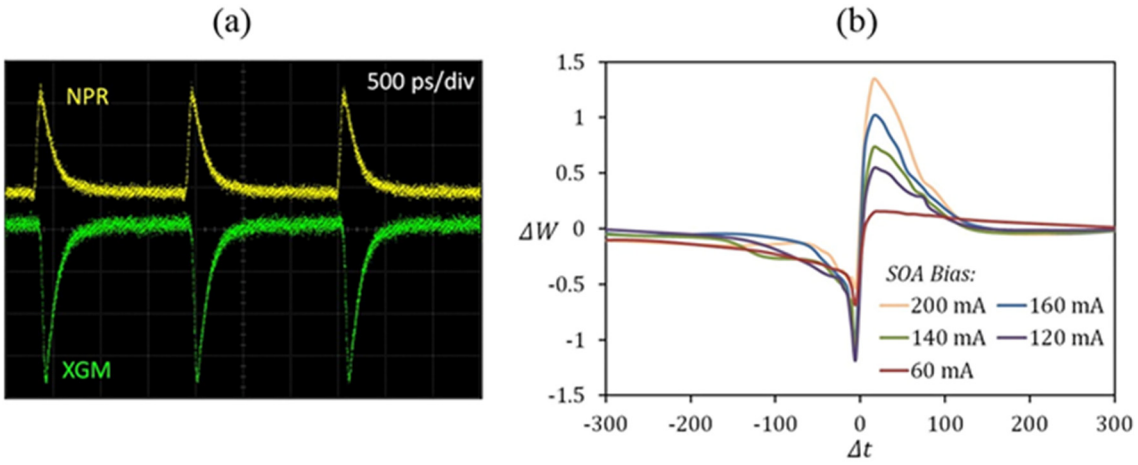

Figure 5.3. (a) Oscilloscope traces of preliminary NPR and XGM results. (b) Experimental STDP results given different SOA driving currents.

Figure 5.3(b) displays the experimental results of the complete STDP experiment, with both pre- and postsynaptic spikes. Considering the low power of CH2, the NPR channel, amplification by 15 dBm was necessary to acquire depression and potentiation windows with similar magnitudes. The normalized STDP curves at various SOA driving currents are presented. Evidently, control over the shape of both windows is achievable by tuning the SOA driving current. As driving current increases, the peak of the potentiation window increases, due to the increase in birefringence induced by higher-amplified pulses; however, the width of the potentiation window remains relatively constant, likely due to the fact that higher driving currents result in quicker restoration of the device's original birefringence. The increasing NPR response and decreasing recovery time compete, serving to maintain the potentiation window's

width across increasing driving currents. As for the depression window, increasing the driving current and consequently decreasing the recovery time, serves to decrease the window's width, while maintaining the depth over increasing driving currents. The presented method of producing an STDP response can be used to demonstrate ultrafast learning in a photonic neuron, as presented in other works with different STDP setups [12].

Angle of Arrival Localization Based on Neuronal Learning Behavior

One of the motivations in exploring neuromorphic engineering systems is the possibility of discovering novel techniques or algorithms that prove useful in advancing other engineering applications. One such manifestation of this motivation, the STDP-inspired AOA system, is presented in this letter. The proposed system, shown in Fig. 4(a), consists primarily of two CW sources at λ_{pre} and λ_{post}, two Mach-Zehnder modulators (MZMs), two microwave antennae, and the described STDP system.

A microwave signal at a frequency f_{RF} is emitted by a transmitter, and is received by two antennas at the AOA circuit, passing through impulse generators and arriving at each MZM. Due to the path difference between the transmitter and each of the two antennas, the received signal experiences different phase shifts (i.e. time delay) at each antenna. Upon modulation, two optical pulse trains with f_{RF} repetition rates are sent into the STDP system. If the optical pulse widths aren't sufficiently small, a number of different methods could be implemented to compress the pulses, depending on f_{RF} and the impulse generators [39-41]. The initial phase difference of the received microwave signals translates to a time delay between optical pulses entering into the STDP system. The STDP circuit produces a unique power output for negative and positive values of Δt, ranging from $-t_m = -d/c$ to t_m, where d is the antenna spacing, and c is the propagation speed. The ability of producing a unique output for both negative and positive

values of Δt eliminates the ambiguity arising from the measurement of signals arriving from opposite directions but at the same angle relative to the antenna array. Consequently, angles between 0˚ and 180˚, corresponding to delays of $\pm t_m$, are distinguishable in this AOA scenario. The measured angle θ of an AOA array is indicated in the Figure 5.4(a) inset, corresponding to different time delays Δt. The normalized STDP output corresponds to a particular delay, which is used to determine the angle through the simple relationship, $c \cdot \Delta t = d \cdot \cos\theta$.

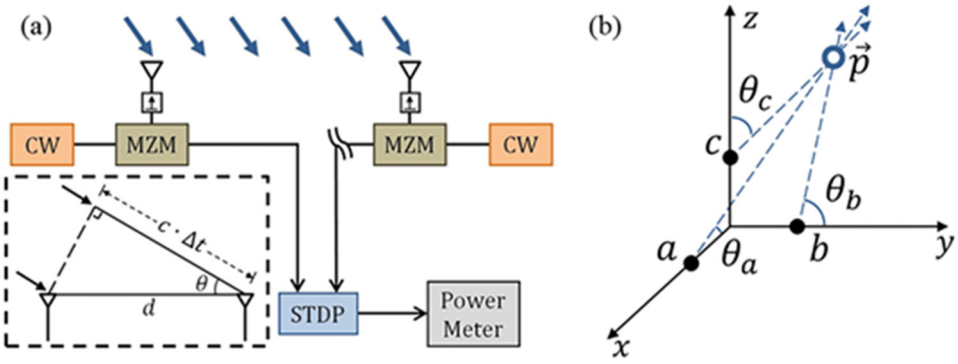

Figure 5.4. (a) STDP AOA array, with AOA response depicted in the inset. (b) Basic 3D AOA localization schematic with three nodes uncovering three directions, θ_a, θ_b, θ_c.

It should also be noted that the operating frequency range of an AOA array is limited by the antenna spacing, d. Considering the periodic nature of the received signal, the maximum possible signal frequency is determined by the relationship, $f_m = c/2 \cdot d$, where f_m is the maximum frequency. For any higher frequency, the STDP circuit is not guaranteed to perform its measurement on the proper set of two pulses, as ambiguity exists between which pulse is "pre" and "post" in a continuous pulse train. The previously explained STDP setup is limited to frequencies below approximately 1.66 GHz, with d at 9 cm. To achieve higher operating

frequencies, the antenna spacing can be decreased, provided that the resulting Δt values are greater than the SOA recovery time.

Furthermore, this individual AOA measuring unit shows promise in being implemented in a 3D localization scheme, as depicted in Figure 5.4(b). The primitive, simulated system consists of three STDP-based AOA arrays, each positioned on a Cartesian axis at (x_a,0,0), (0,y_b,0), and (0,0,z_c) at points a, b, and c respectively. Each array's AOA value, θ_a, θ_b, and θ_c, contributes to constructing a simple set of nonlinear equations, three conical surfaces, shown below,

$$(x_0 - x_a)^2 = cot^2\theta_a \cdot ({y_0}^2 + {z_0}^2),$$

$$(y_0 - y_b)^2 = cot^2\theta_b \cdot ({x_0}^2 + {z_0}^2),$$

$$(z_0 - z_c)^2 = cot^2\theta_c \cdot ({x_0}^2 + {y_0}^2),$$

from which a microwave transmitter's location at (x_0,y_0,z_0) can be determined. Two primary sources of error, measuring unit location error and laser instability, are considered in the AOA and 3D localization simulations.

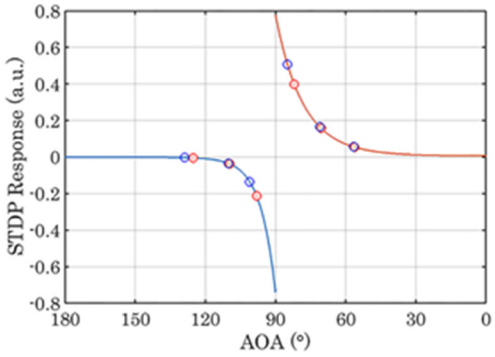

Figure 5.5. Comparison of expected (red) and observed (blue) STDP outputs for nodes at x_a = 0.5, 5, 8, 12, 15, and 20 m.

For the AOA system simulation, the STDP measuring unit is receiving a microwave signal from a transmitter at known location, (x_0,y_0,z_0), in meters. Figure 5.5 illustrates the expected (red filled) and observed (blue outlined) STDP output for a node at x_a = 0.5, 5, 8, 12, 15, and 20 m, with the furthest right pair corresponding to x_a = 0.5 m, and the furthest left pair corresponding to x_a = 20 m. The expected (red) points represent ideal outputs free of error, and the blue points represent outputs when the system is subjected to error. The transmitter is located at an arbitrary point, (10,10,10), and error in the form of unit displacement and laser power fluctuations is considered. For an indoor wireless localization system, unit displacement would be low, so a 1 mm error is considered. The other contribution to the error of the observed STDP output is 0.003 dBm of laser power error, as the DFB laser used for CW generation in our STDP experiments claims such levels of power instability. The results depict the AOA error for different angles, indicating larger expected errors for angles near to 0˚, 90˚, and 180˚.

The device's performance in locating a transmitter at the same point, (10,10,10), is shown in Figure 5.6, which illustrates error plots for the unit's AOA measuring ability when considering a range of unit displacement and laser power fluctuations of up to 1 mm and 0.003 dBm, respectively. Each error plot presents the root mean square error (RMSE) of the device's AOA measurement in degrees, with respect to variance in the forms explained above. As illustrated in Figure 5.6(a), even with maximum variance in both node location and laser power, the relative AOA measurement errors for a measuring unit located at (1,0,0) and a transmitter located at (10,10,10), both in meters, do not exceed 0.5˚. Furthermore, by relocating the node to (3,0,0), illustrated by Figure 5.6(b), the maximum RMSE can be decreased to approximately 0.425˚. As the detected AOA approaches 90˚, measurement error due to laser instability continues to decrease while error due to offset variance begins to dominate, shown by Figures 5.6(c) and

5.6(d) for nodes at (5,0,0) and (7,0,0). For each of the four scenarios, the STDP AOA array outperforms previously explored photonics-based AOA devices, which report errors of ±2.5º [38].

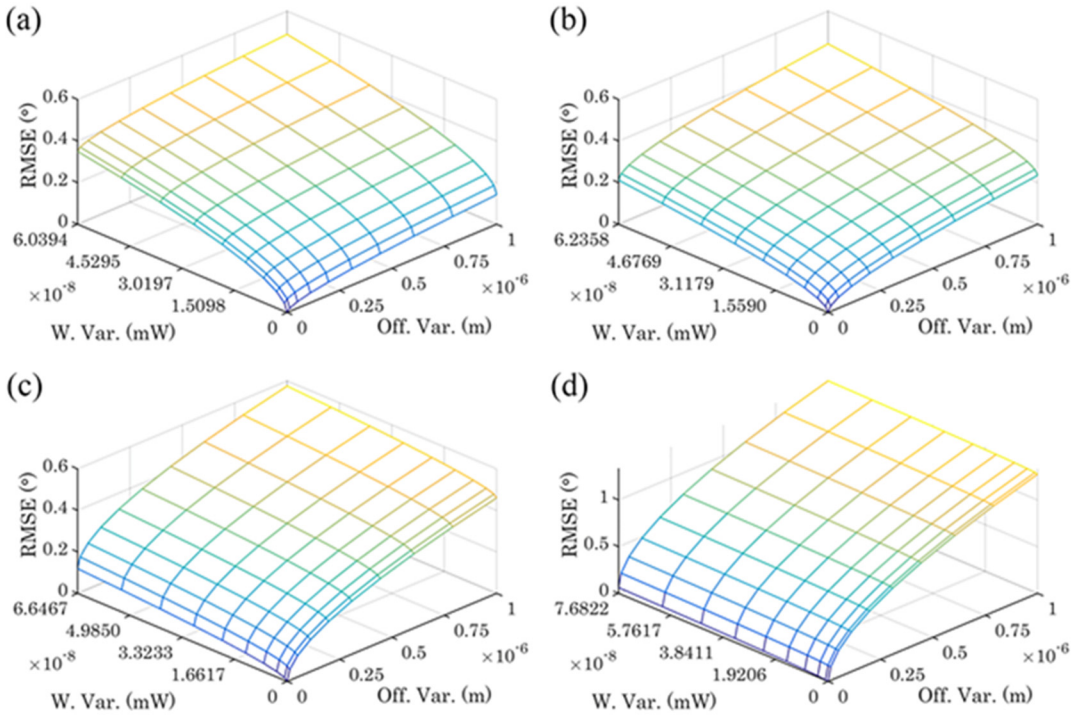

Figure 5.6. (a) Error plot for an AOA node at (1,0,0) detecting a transmitter at (10,10,10); (b) AOA error plot for a node at (3,0,0); (c) AOA error plot for a node at (5,0,0); (d) AOA error plot for a node at (7,0,0).

The error plots for the full 3D localization scheme are presented in Figure 5.7. With a maximum location error of 1 mm and laser instability of 0.003 dBm for each node, the RMSE, in meters, of the transmitter location is at most just over 1 m, occurring when the AOA arrays are located at $x_a = y_b = z_c = 1$ m. By relocating two of the nodes to $y_b = z_c = 5$ m, the maximum RMSE is decreased to 0.4 m. Considering the same error values and nodes at $x_a = y_b = z_c = 5$ m,

a maximum RMSE of about 0.3 m is acquired and can be reduced even further to 0.15 m by positioning the nodes at $x_a = y_b = z_c = 15$ m. The measurements report accuracies that rival that of the most accurate indoor positioning systems, which are all significantly more complex and expensive than the photonic setup presented, with their large networks of measuring units [33-35]. The presented setup relies solely on the three measuring units and achieves comparative accuracies for much larger distances between transmitters and receivers. Beyond the indoor realm, a RMSE of 9.7 m is possible with nodes located at $x_a = y_b = z_c = 5$ m, given the same error sources, when detecting a transmitter at over 100 m. This reasonable error indicates the possibility of developing such a device for outdoor positioning purposes as well.

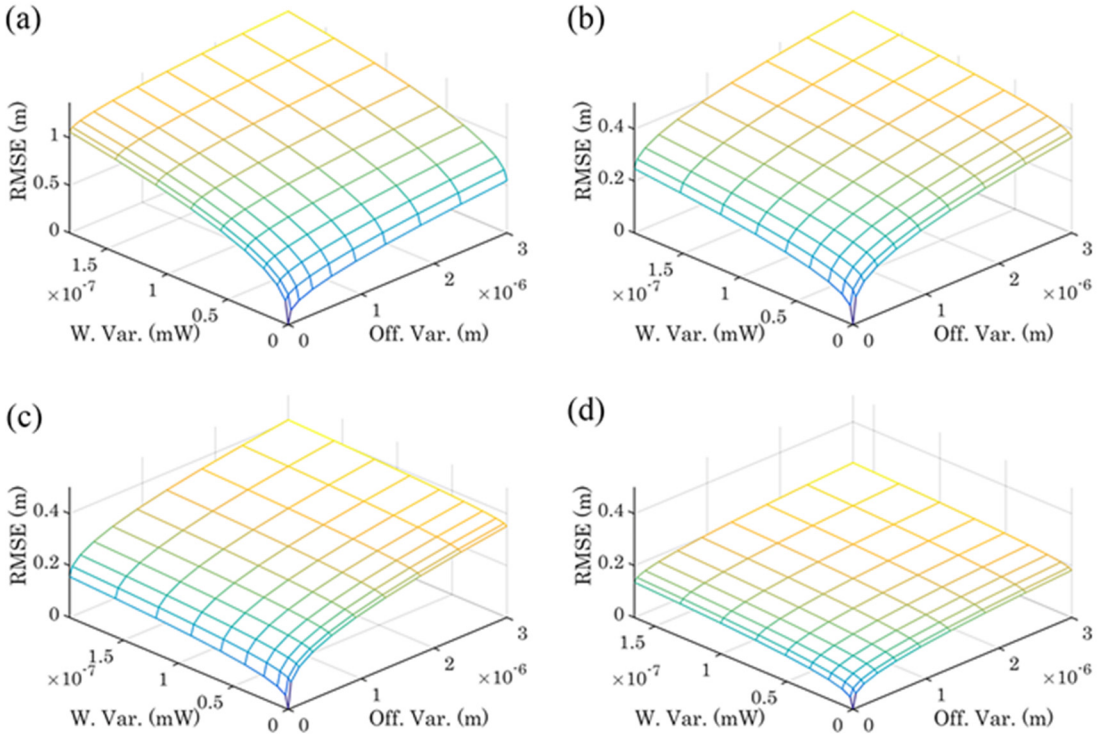

Figure 5.7. (a) Error plot for detecting a transmitter at (10,10,10) with nodes at $x_a = y_b = z_c = 1$ m; (b) Error plot with nodes at $x_a = 1$ m, $y_b = z_c = 5$ m; (c) Error plot for nodes at $x_a = y_b = z_c = 5$ m; (d) Error plot for nodes at $x_a = y_b = z_c = 15$ m.

Conclusion

The biological STDP algorithm has been successfully demonstrated optically using XGM and NPR cooperatively in a single SOA, and the device presented could be implemented in previously developed photonic learning systems. Furthermore, these primitive simulations illustrate the potential application of STDP photonic systems in AOA localization schemes. By solving simple nonlinear equations constructed from AOA information drawn from relatively simple photonic systems, tolerable localization accuracy is acquired for a range of transmitter distances of up to 100 m, when considering reasonable error sources and different node arrangements. Devising a highly accurate AOA system can be difficult due to the challenges presented by shadowing or multipath reflection. For a photonic system however, another technique often employed in photonic neuromorphic systems could be implemented to overcome these difficulties. Through use of an optical thresholder, all incident signals below a particular threshold could be effectively suppressed, without affecting the desirable ones [14,42]. All detected signals resulting from multipath reflection would be weaker than the desirable signal and consequently eliminated. Considering the role that node location relative to transmitter location plays in AOA accuracy, a modified system with a larger distribution of measuring units would exhibit higher accuracy and provide uniform precision for transmitter localization within the region.

CHAPTER 6

JAMMING AVOIDANCE RESPONSE

Introduction

The prevalence of wireless devices and the progression of communications technology have facilitated the vision of anytime, anywhere access to wireless networks. Ubiquitous access has recast modern communication and introduced a new level of strain on networks, making such systems more susceptible to radio interference and jamming. Traditionally, the Federal Communications Commission (FCC) has controlled the radio frequency spectrum in an effort to minimize these issues by allotting bands to different applications and users, including commercial, defense, and civilian applications [43,44]. The radio frequency spectrum is a scarce resource for both licensed and unlicensed applications. Considering the recent boom in wireless technologies, those unlicensed bands left open for public use are often over-crowded and consequently suffer from radio interference, which is difficult to mitigate due to the wide range of devices that operate at such frequencies. Further licensing of personal devices would aid in minimizing interference; however, it would severely reduce the flexibility of the public bands. The frequency ranges open for personal and commercial use are limited, and placing additional restrictions could prove too complex of a task that leads to further complications. Whether for licensed or unlicensed frequency bands, a dynamic approach to managing spectrum scarcity, as opposed to static spectrum allocation, is ultimately necessary if efficiency of spectrum use is to be maximized.

Dynamic spectrum access, opportunistic spectrum access, spectral partitioning, and channelizing represent proposed approaches towards tackling this issue, but all require some degree of control communication between devices, which could similarly be impacted by interference due to overcrowding [45-50]. Another major research focus, cognitive radio, involves the use of weak probe signals that scan the spectrum for "spectral holes," regions of the spectrum not being actively used [49]. Spectrum sensing over a large bandwidth is difficult, however, due to difficulties arising from avoiding interference caused by the probing with an individual device over a range of frequencies.

The approach presented here, one that avoids the possibility of causing interference through probing and does not require comprehensive spectral scanning, is inspired by the neural circuitry of the Eigenmannia, a genus of fish. The Eigenmannia use electrolocation to determine their surroundings by generating electric fields and detecting disturbances in the fields caused by nearby objects [51-53]. For these creatures, their ability to effectively make sense of their surroundings is a life or death necessity, and their neural circuitry has evolved to reflect this. An individual fish emits and receives a low frequency electrical signal in the kilohertz range, is simultaneously able to sense the frequency output of other nearby Eigenmannia, and automatically regulates its own frequency in an effort to avoid interference. This regulation of frequency, known as the Jamming Avoidance Response (JAR), represents a method of uncoordinated communication that could be applied in modern wireless systems, eliminating the need for further restriction of the unlicensed FCC bands and allowing for maximum spectrum efficiency in all bands [54]. The ability for an individual unit to adjust its output frequency based on observed interference requires no direct coordination with other units in the system, and is therefore ideal for the cluttered complexity that defines unlicensed frequency bands. The JAR

approach towards detecting and using spectral holes is a practical means of solving a physical problem that avoids indirectly, incompletely mitigating the issue by managing networks with excessive protocol.

A photonic approach to JAR is ideal considering the flat frequency response of photonic devices in the terahertz range [55], their electromagnetic (EM) immunity, and near-instantaneous response times. The uniform frequency response is of particular importance in this scenario considering the lack of a priori knowledge of which frequencies are available in a system. Furthermore, processing of unknown signals in the radio frequency (RF) range is not efficient and often impossible electronically due to the bandwidth limitation and precise design required in electronics for different frequency bands. On the other hand, it is possible to be done optically due to the consistent performance of optical equipment over a wide range of frequencies. In this work, a primarily photonic JAR circuit is developed through simulation using linear and nonlinear optical effects and techniques used in photonic neuromorphic processing systems. The device serves as a primitive example of a solution to the spectral scarcity issue that will continue to build in severity if not handled on the physical level.

Eigenmannia Jamming Avoidance Response Circuitry

As previously stated, the Eigenmannia genus represents a categorization of weakly electric fish that use electrolocation as a means of sensing and moving through their surroundings in the ocean [51-53]. An Eigenmannia fish does so by discharging an electrical signal at a particular frequency in the kilohertz range and then detecting its own discharge, with perturbations in its electrical field indicating different objects [51,54]. If another fish is nearby and emitting a signal at a similar frequency, both fish's ability to electrolocate is hindered due to interference. Accordingly, their neural circuitry is able to process amplitude and phase

information of the interference signal, determine whether it's higher or lower in frequency relative to the fish's own discharge frequency, and then automatically shift its discharge to a different operating frequency [54]. Interestingly, this adjustment is always made in the proper direction, i.e. the operating frequency will be lowered if the interfering signal is higher in frequency than the reference. This implies that the process is not one of haphazard, random switching but a systematic response to accurate information drawn from the detected interference waveform.

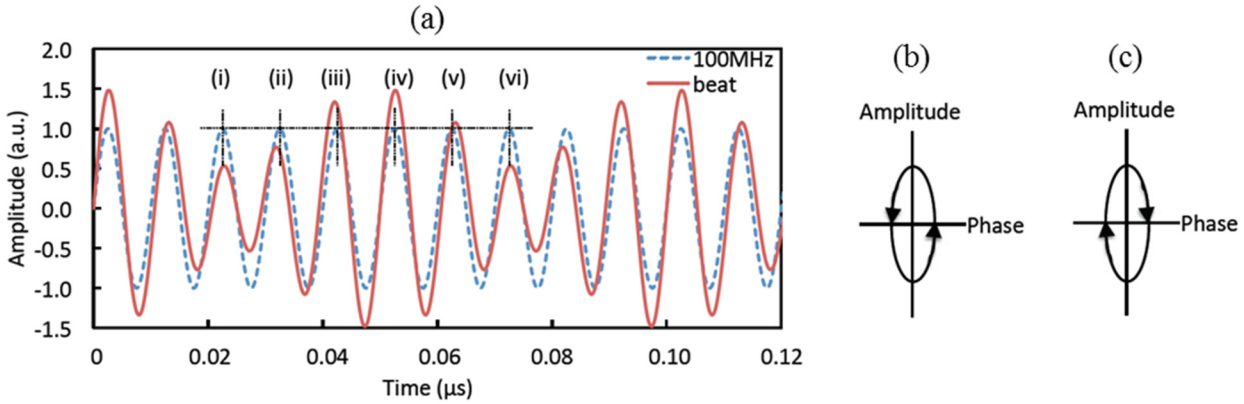

Figure 6.1. (a) Illustration of a 20 MHz beat in red, alongside a 100 MHz reference sinusoid (blue dashed line), generating from the reference beating with an 80 MHz sinusoid. (b) Amplitude vs. phase plot showing counterclockwise rotation, indicating that the interfering frequency is higher than the reference frequency. (c) Amplitude vs. phase plot showing clockwise rotation, indicating that the interfering frequency is lower than the reference frequency.

The process by which JAR takes place is most easily described by a phasor phenomenon [56]. When a sinusoid signal at frequency f_1 interferes with another sinusoid signal of similar frequency f_2, a beat envelop signal results at a frequency $|f_b| = f_1 - f_2$. As illustrated by Figure

6.1(a), the individual peaks of a 20 MHz beat rotate clockwise around the peaks of a 100 MHz reference signal if the interfering signal is at a lower frequency of 80 MHz (i)-(vi). Figure 6.1(b) plots amplitude with respect to phase, illustrating counterclockwise rotation for the case in which the interfering frequency is higher than the reference frequency, and Fig. 6.1(c) illustrates the clockwise rotation resulting from an interfering signal at a lower frequency relative to the reference. Evidently, the rotation direction uniquely determines the sign of the frequency difference.

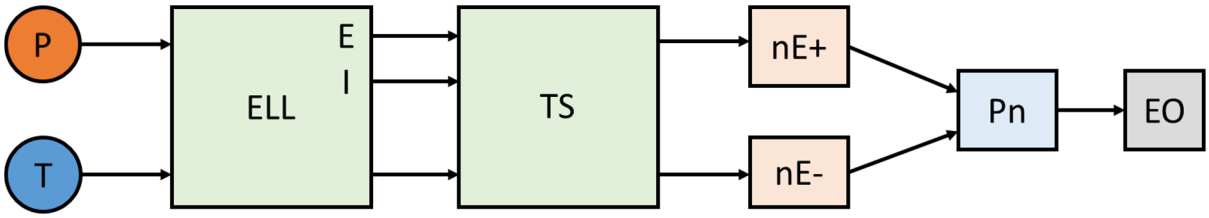

Figure 6.2. A simplified schematic of the Eigenmannia JAR circuitry, with the P, T, E, and I-units, the Electrosensory Lateral Line lobe (ELL), the Torus Semicircularis (TS), Nucleus Electrosensorius (nE), Pacemaker nucleus (Pn), and the electric organ (EO). The P, E, and I-units convey beat amplitude information and the T-unit and components of the TS convey phase information. Logic performed by other TS elements excite the nE+ or nE- neurons, increasing or decreasing the frequency of the discharge regulated by the Pn, and ultimately transmitted by the EO.

The simplified Eigenmannia JAR neural circuitry is depicted in Figure 6.2, beginning with two different types of electroreceptors located on the body's surface, the T-unit and the P-unit [51]. The P-unit is primarily responsible for interpreting information about the amplitude of beat signal and consists of a cluster of neurons that fire rapidly when the beat is increasing in

amplitude and fire slowly when the beat is decreasing in amplitude. The T-unit neurons process phase information of the reference signal by firing at every positive zero crossing point of reference discharge. The receptors' outputs are both sent to the Electrosensory Lateral Line lobe (ELL), in which the amplitude and phase information are independently processed. A rapid firing rate of the P-unit results in the E-unit firing and a slow firing rate results in the I-unit firing. Furthermore, the ELL serves to reduce any timing jitter of phase information arriving from the T-unit, before then sending it to the Torus Semicircularis (TS) alongside the E-unit and I-unit spikes.

Table 6.1. Summary of the JAR logic decision based on amplitude and phase information.

P-Unit (Beat Amplitude Information)	TS (Phase Information)	JAR Decision (Frequency Adjustment)
Increasing	Leading	Increase
Increasing	Lagging	Decrease
Decreasing	Leading	Decrease
Decreasing	Lagging	Increase

By comparing the positive zero crossing points within the beat signal to that of the reference signal, the TS is able to determine whether the interfering signals' crossing points are leading or lagging the reference crossing points by outputting different spiking patterns. The unit then performs a logical operation on the lead/lag information and the increasing/decreasing amplitude information, from which it decides whether to increase or decrease the fish's discharge frequency by stimulating the Nucleus Electrosensorius (nE+ and nE-) and ultimately the Pacemaker nucleus (Pn), which sets a new output frequency to be transmitted by the electric organ (EO). The TS decision based on the multiple inputs is summed up by Table 1, which

compares the decision with its input amplitude and phase information, indicating an XNOR or XOR behavior. Figure 6.3 illustrates the TS operation principle given an original reference frequency of 100 MHz, with Figure 6.3(a) portraying the scenario in which the interfering signal is at 80 MHz, and Figure 6.3(b) depicting the scenario in which the interference is at 120 MHz. As can be seen, the nearest positive zero crossing point of the beat is leading the nearest crossing point of the reference sinusoid at the rising edge and trailing at the falling edge of the beat in Figure 6.3(a). The opposite trend is displayed in Figure 6.3(b) for an interfering frequency greater than the reference frequency. The optical implementation of this neural circuitry is described in the following sections, which makes use of several different signal processing techniques towards determining beat amplitude information and interfering signal phase information.

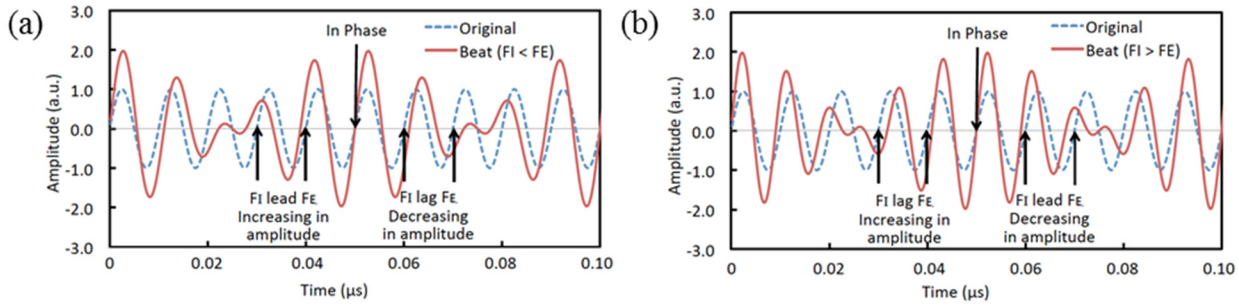

Figure 6.3. (a) Illustration of the JAR logic operation, when (a) the interfering frequency FI is lower than the reference frequency FE, and when (b) FI is higher than FE. The beat signal and reference signal are shown as the red and dashed blue curves, respectively. In both figures, arrows point to different reference positive zero crossing points in which the interfering signal is either leading or lagging the reference signal in phase, and the beat is either increasing or decreasing in amplitude.

Photonic Jamming Avoidance Response Circuitry

The basic understanding of the Eigenmannia JAR neural circuitry serves as a rough guideline for developing the photonic equivalent, which can be seen in Figure 6.4. Considering that the reference frequency of most wireless transmitters is readily available from the local oscillator (LO), some adjustments to the model have been made. As can be seen, the reference signal would be split and sent to the transmitter and to the T-unit directly, and the ELL representative no longer processes information from both the T-unit and P-unit. Thus, the photonic circuit is divided into four major elements:

(a) P-unit: This unit consists of an envelope detector and a circuit that detects the rising edge of the beat envelope and emits an optical pulse correspondingly.

(b) T-unit and ELL: This subsystem works to fire spikes at every positive zero crossing point of the transmitter's output sinusoid.

(c) TS: The TS receives input directly from the receiver in the form of two beating RF signals and from the T-unit and ELL in the form of a train of spikes temporally indicating the positive zero crossing points of the transmitter signal. The unit uses optical effects to determine whether the interfering signal zero crossing points are leading or lagging the reference signal's zero crossing points and spikes accordingly.

(d) Logic gate: The final processing element interprets the phase and amplitude information from the previous units and decides whether the transmitter should increase or decrease its output frequency. This information instructs the signal generator and the transmitter output is properly adjusted.

The proposed system is simulated by the optical communications simulation software, OptiSystem, and demonstrates how it would operate around the 2.4 GHz band in a wireless setting. The following sections detail the introduced subsystems employed.

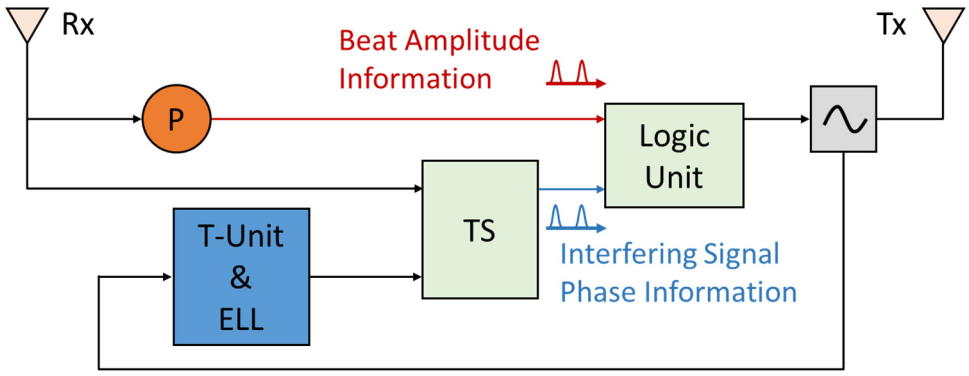

Figure 6.4. A simple schematic for the photonic JAR circuit, with receiver and transmitter, Rx and Tx, respectively, the P-unit for interpreting beat amplitude information, the T-unit for indicating the positive zero crossing points of the reference signal, the TS for determining the phase of the interfering signal relative to the reference signal, the logic unit for interpreting the phase and amplitude information, and the local oscillator, indicated by the gray box with a sinusoid, for generating the reference signal.

P-unit – For the detection of rising edge of the beat signal

The overall system, as illustrated by Figure 6.4 receives its own transmitted RF signal and an interfering signal from an unknown location by means of an antenna, and each signal is sent to the P-unit where envelope detection is first performed to extract the beat frequency. Then, the beat and its inverted counterpart are converted to the optical domain where processing based on temporal offset and signal subtraction is performed. Ultimately, the P-unit emits an optical pulse at the rising edge of the envelope, and the resulting train of pulses is sent to the logic

circuit along a precisely determined length of optical fiber. Figure 6.5 presents a diagram of the photonic P-unit.

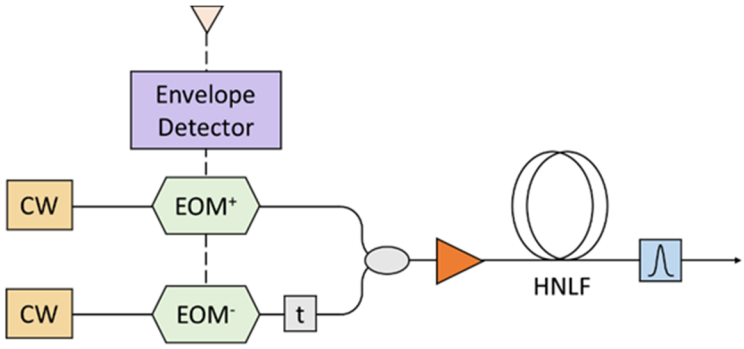

Figure 6.5. P-unit schematic, with two continuous wave (CW) optical sources, two electro-optic modulators (EOM), one positively and one negatively biased, an envelope detector, delay t, optical amplifier indicated by the orange triangle, a length of highly nonlinear fiber (HNLF), and a bandpass filter.

An envelope detector, in its most basic form, is an RC circuit consisting of a diode, a resistor, and a capacitor, in which the capacitor stores charge at the rising edge of the signal, while releasing it slowly on the falling edge through the resistor. The diode performs rectification, allowing current flow in just one direction, and the end result is a signal that appears as a rectified sinusoid at the beat frequency, as illustrated by Figure 6.6. More advanced envelope detectors are commercially available, operating over an array of different frequencies and suited for multiple applications [57-59]. Due to the limitations of OptiSystem and the relatively simple nature of envelope detection, simulation of the envelope detection is not necessary and the resulting signal is generated independently.

The extracted envelope is split into two branches and converted to an optical signal through use of two electro-optic intensity modulators (EOM), one positively biased and one

negatively biased so that a non-inverted copy and an inverted copy of the signal are obtained. The EOM is an essential electro-optic device that consists of two phase modulators to achieve amplitude modulation through interference. In an EOM, an input optical signal is split between two branches, each containing a phase modulator. The phase modulator's index of refraction is a function of the strength of an applied varying electric field, which in this case is the amplitude-varying envelope signal. Due to the varying index of refraction, the input continuous wave (CW) optical signal experiences a time-varying phase delay. Consequently, when the optical signals of both branches in the EOM are recombined, they interfere and reproduce the modulated signal in the optical domain. Depending on the sign of an externally applied bias voltage, the resulting modulated signal is either upright or inverted.

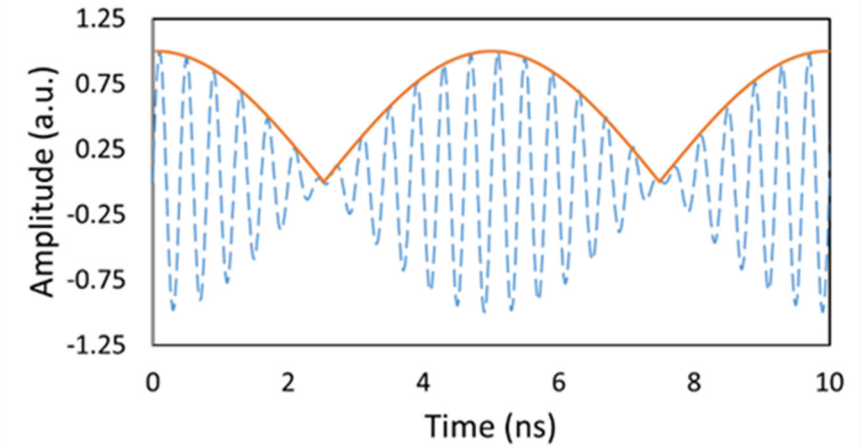

Figure 6.6. Envelope detection in the first stage of the P-unit. The beat of two signals at 2.4 and 2.6 GHz is shown by the blue dashed curve, and the signal after envelope detection is indicated by the orange curve.

The two P-unit branches are slightly offset, such that a slight temporal delay of 1.5 ns is experienced in the negatively-biased EOM branch before the two optical signals at 1551 and

1552 nm, respectively, are combined at a fiber coupler, where their intensities are added together. For example, two optical signals modulated by an envelope corresponding to a beating 2.4 and 2.425 GHz signal are shown in Figure 6.7(a) alongside the signal after the coupler. Figure 6.7(b) depicts the same information but for a 240 MHz signal, corresponding to the beating between a 2.4 and 2.64 GHz signal. The positively biased EOM optical signals are shown in green, the negatively biased EOM signals are shown in red, and the signals after coupling are shown in gray.

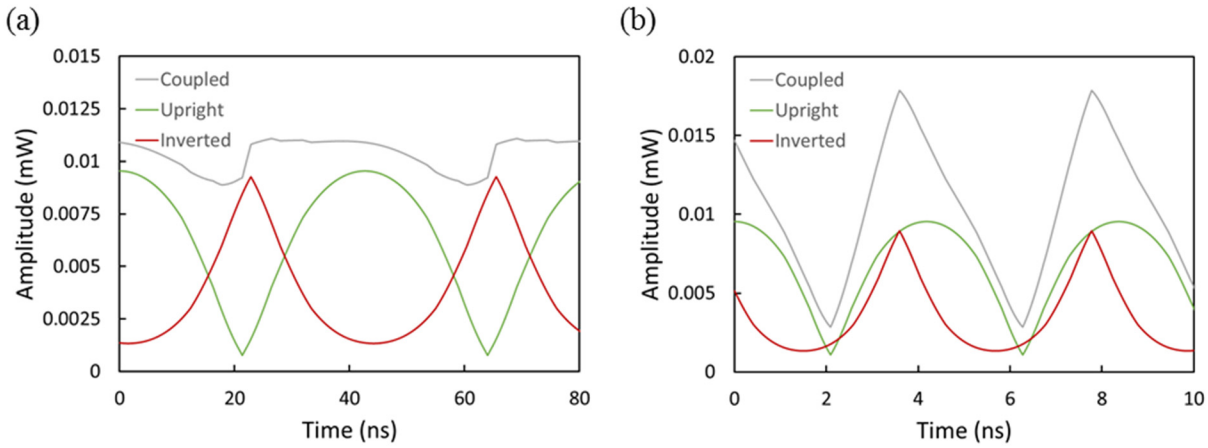

Figure 6.7. Depicts beats modulated onto optical carriers, one upright (green) and the other inverted and delayed (red) for: (a) the 25 MHz beat of 2.4 and 2.425 GHz signals and (b) the 240 MHz beat of 2.4 and 2.64 GHz signals. After coupling, the linearly added intensities produce the signal shown in gray for both cases.

The final element in the P-unit is a 10 m length of highly nonlinear fiber (HNLF), in which the nonlinear optical effect of four-wave mixing (FWM) is utilized to produce a pulse at the rising edge of the beat, as the signals after coupling, shown in gray in Figure 6.7, do not maintain the same pulse shape over the range of beat frequencies, and further processing is

needed for the device to emit a proper pulse. The processing technique used, FWM, occurs when at least two signals at different frequencies, ν_1 and ν_2, propagate through nonlinear media and produce two additional frequency components at $\nu_3 = \nu_1 - (\nu_2 - \nu_1)$ and $\nu_4 = \nu_2 + (\nu_2 - \nu_1)$, where $\nu_2 > \nu_1$, assuming that the inputs are phase-matched. Because of the necessity of high optical power for FWM, the effect only occurs at the rising edge of the beat, where the two optical inputs are of sufficiently high power. The optical amplifier preceding the HNLF is initialized for lower frequency beats, which correspond to small separation between the reference and interfering signal, such that output of the P-unit is a spike temporally aligned to the crossing point between the two optical signals. Near this crossing point, the power of each signal is sufficiently high to induce a noticeable FWM effect, and a 0.3 nm bandpass filter centered at 1550 nm passes one of the FWM products, as indicated by Figure 6.9(a) for a 25 MHz beat envelope. For higher beat frequencies, the fixed 1.5 ns delay shifts the inverted signal further along the rising edge of the envelope in terms of relative phase. This leads to a minor relative phase shift in the P-unit output for higher frequency signals as the necessary power for FWM is effectively satisfied at all times corresponding to the peak amplitude of the inverted signal. This trend is further supported by the fixed bias current supplied to the amplifier and is pictured in Figure 6.9(b) – 6.9(e), showing the P-unit's output for beat frequencies of 50, 100, 200 and 240 MHz. In each of the figures, the vertical axis corresponds to the P-unit spike shown in gray, and the initial envelopes, displayed in blue and orange, are scaled down for reference. In actuality, the average power of the coupled inputs was approximately 7 dBm for all tested beat frequencies, and the average output powers of the P-unit were -12, -10.3, -7.8, -7.7, and -7.5 dBm for the 50, 100, 200, and 240 MHz beats, respectively.

Considering that operation of the JAR circuitry is not necessary for frequencies sufficiently far apart, a 250 MHz bandpass filter is positioned after envelope detection, preventing the modulation of any beat signal larger than this frequency onto the optical carriers. In such a scenario the two optical signals then fail to initialize FWM, and the P-unit entirely stops spiking – disabling the JAR operation. Figure 6.8(a) shows a 280 MHz envelope before and after a low pass filter, and Figure 6.8(b) shows the consequent P-unit output. Evidently, conversion of the envelope to the optical domain fails, resulting in no output from the P-unit. Also, this bandpass filter prevents any issues related to the fixed delay line from arising, as for beats larger than ~333 MHz the delay would align the peak powers of the two optical signals, resulting in spikes corresponding to the beat's peak. Such behavior would result in ambiguity between the beat's rising and falling edge, and the unit would output a spike at the beat's falling edge for frequencies just larger than ~333 MHz.

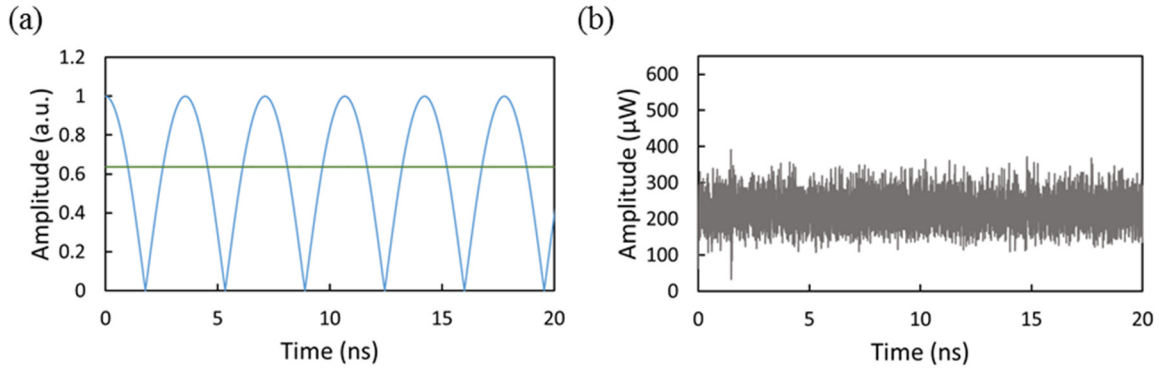

Figure 6.8. 250 MHz low-pass filter preventing the P-unit from spiking at the rising edges of a 280 MHz beat. (a) The 280 MHz beat is indicated by the blue curve prior to filtering and the straight green line represents the signal after the filter. (b) The P-unit does not spike as FWM fails to occur.

Ultimately, figure 6.9 shows the P-units ability to properly spike for frequency separations ranging from 25 to 240 MHz, based on a fixed temporal delay, FWM, and optical filtering of one of the FWM generated frequencies, which is only able to occur at the rising edge of the beat signal. The output's tendency to shift towards the beat peak at higher frequencies, such as 240 MHz, results in a minor temporal misalignment between inputs at the logic stage of the JAR circuitry, but the error appears inconsequential, as indicated later by Figure 6.13.

Figure 6.9. P-unit outputs, with FWM products shown in gray and beat modulated optical signals shown in blue and orange, for interfering and reference signal separations of: (a) 25 MHz, (b) 50 MHz, (c) 100 MHz, (d) 200 MHz, and (e) 240 MHz.

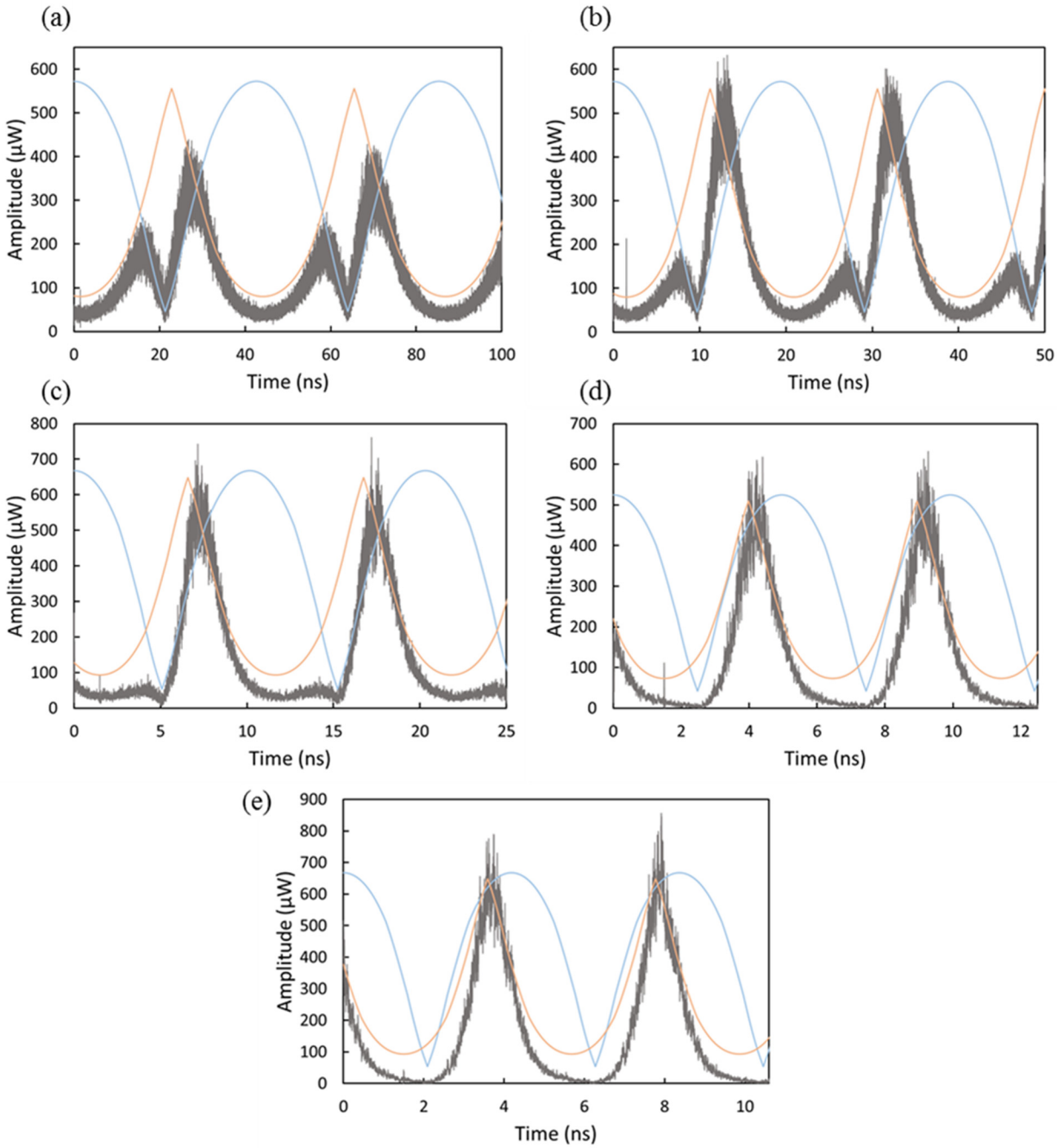

T-unit and ELL – For the detection of the reference signal's positive crossing points

This system, as depicted by Figure 6.10, receives a copy of the reference signal directly from the local oscillator, and, because of the fixed distance between the transmitting and receiving antennae, the length of the fiber from the local oscillator is set so that the reference signal from the oscillator is in phase with the reference signal transmitted and received by the antennae at a later point in the overall system. The system then locates the positive zero crossing points of the reference signal by means of amplitude clamping, self-phase modulation (SPM), and spectral filtering.

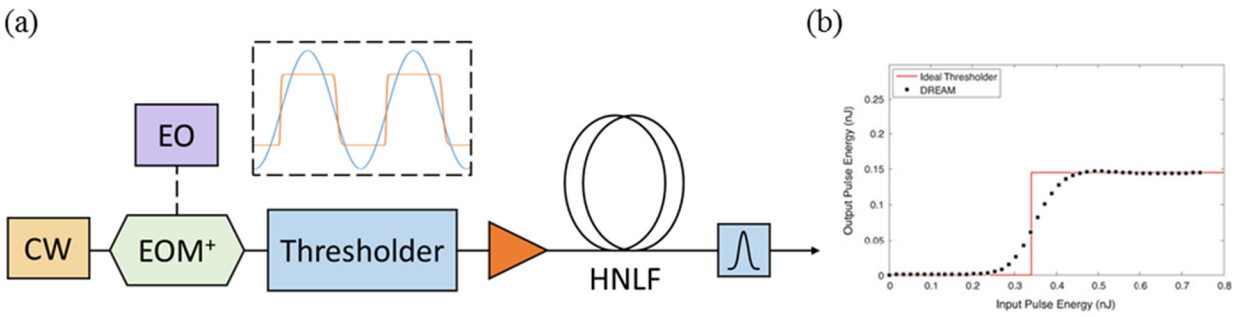

Figure 6.10. (a) T-unit and ELL schematic, with a CW source modulated by an EOM receiving the reference signal directly from the EO. A NOLM-based thresholder performs amplitude clamping, as shown by the inset in the dashed box. An optical amplifier and bandpass filter are indicated by the orange triangle and small blue box, respectively, and a length of nonlinear fiber is labeled HNLF. (b) DREAM thresholder transfer function, comparing input and output powers of 10 ps pulses. A similar device would be used for amplitude clamping.

For the first step in this process, the reference sinusoid passes through an optical thresholder, similar to those implemented by photonic LIF neuron models, with transfer functions similar to that of Figure 6.10(b) [10,42]. As previously described, the device works to

suppress signals below a set power threshold and pass those beyond the threshold with a sigmoidal transfer function. Consequently, the sinusoid is clamped in such a way that its crests and troughs are flattened, while the rising and trailing edges are made steeper [42]. To surpass simulating the amplitude clamping effect, non-return-to-zero (NRZ) pulses of appropriate width are generated electronically at the same rate as the reference signal frequency and converted to the optical domain using another EOM to modulate the signal onto a 1550 nm continuous wave.

The leading edges of these NRZ pulses are roughly aligned in time with the positive zero crossing points of the reference sinusoid, and a filtering technique similar to NRZ-to-PRZ (pseudo-return-to-zero) signal conversion is used to extract these edges. Considering the inherent nonlinear properties of fiber, an NRZ signal induces a minor red shift in its leading edge and a minor blue shift in its trailing edge, and NRZ-to-PRZ conversion is therefore achieved by filtering out the central wavelength of the signal, leaving narrow pulses at the rising and trailing edges of the original NRZ pulse. By performing a similar technique but instead just filtering out the longer wavelength end of the NRZ pulse's spectrum, extraction of exclusively the leading edge is possible.

The manifestation of this process within the JAR circuit involves first sending the optical NRZ pulses through another length of HNLF, in which SPM occurs, broadening the spectrum and simultaneously inducing further red shifts and blue shifts. SPM is a nonlinear phenomenon describing how a medium's index of refractive changes proportionally to input optical intensity, resulting in a shift towards the longer wavelengths at the leading edge and a shift towards shorter wavelengths at the trailing edge of a pulse. Then, the signal passes through an optical bandpass filter with a 0.3 nm bandwidth centered at 1550.52 nm at the longer wavelength side of the original pulses, and the ultimate T-unit and ELL output is acquired. Figure 6.11 shows the

frequency and time domain simulation outcome for this technique performed on a 2.4 GHz NRZ pulse train with a sinusoid provided for reference in Figure 6.11(b). A train of narrow optical pulses, in synch with the positive zero crossings of the reference signal and at an average power of -7.8 dBm, is emitted and sent to the TS, where phase information is processed.

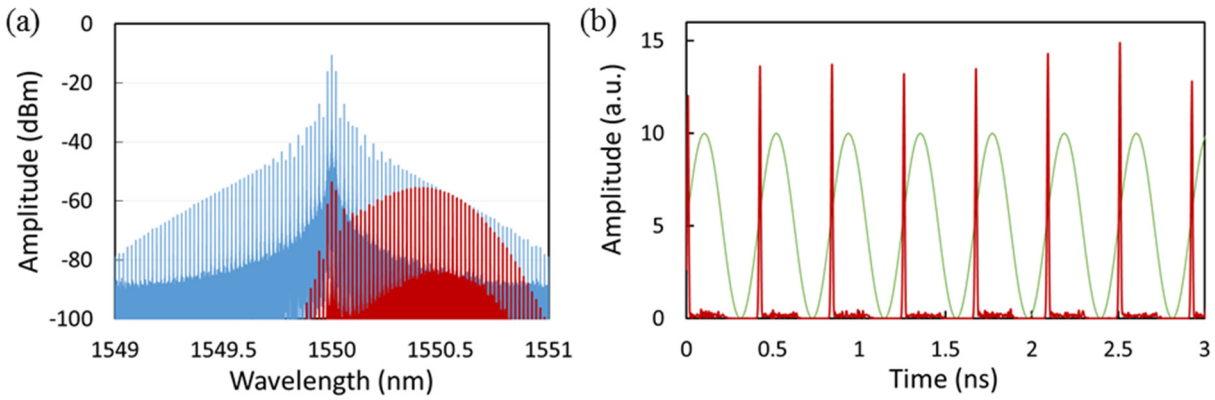

Figure 6.11. T-unit and ELL results. (a) NRZ pulse spectrum shown in blue, filtered leading edge pulse spectra shown in red. (b) 2.4 GHz positive zero crossing point pulses shown in red with a 2.4 GHz reference sinusoid shown in green.

TS Circuitry – For determine the phase of the interfering signal relative to the reference signal

This simple system, shown in Figure 6.12, receives input from the T-unit and ELL unit and directly from the receiver antenna, consists primarily of an SOA, utilized in a manner representative of an integrator in a photonic neuron, and serves to indicate at which times the interfering signal lags the reference signal in phase. First, the beating signals are converted to the optical domain by an EOM, modulating the interference pattern onto a 1555 nm optical carrier. Then, this new optical signal with an average power of -8.7 dBm is sent to the SOA alongside the positive zero crossing pulses (attenuated to an average power below -25 dBm) at 1550 nm, which act similarly to the sampling pulses of an LIF photonic neuron. A 2 nm bandpass filter centered at 1550 nm then passes the sampling pulse train, whose pulses' amplitudes are altered by XGM, as described in the LIF photonic neuron section of Chapter 2.

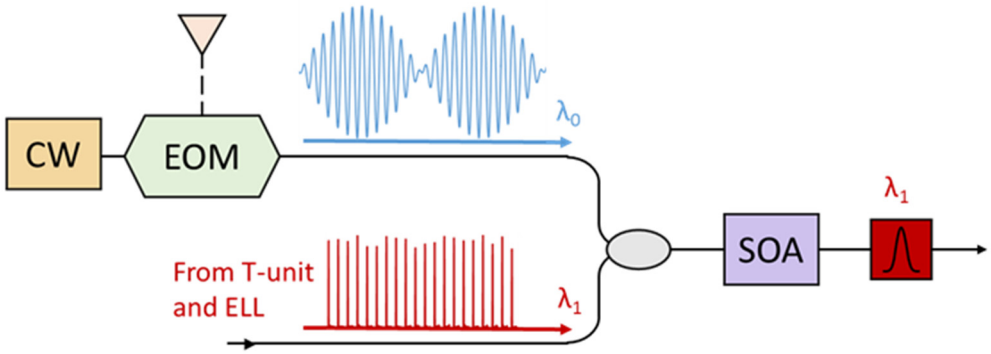

Figure 6.12. The TS unit, showing the received signal (blue curve) modulated onto a CW optical carrier at λ_0 by an EOM and the pulse train at λ_1 generated from the T-unit and ELL (red curve). Both inputs are coupled together and sent to an SOA, and a bandpass filter at λ_1 passes the pulse train. Ultimately, the unit's output indicates at which points the interfering signal is lagging behind that of the reference.

Figure 6.13 shows both inputs for two different scenarios, in which the interfering signal is either 100 MHz above (Figure 6.13(a)) or below (Figure 6.13(b)) a 2.4 GHz reference signal. As can be seen from Figure 6.13(a), the pulses are temporally closer to the individual peaks in the beat signal at the rising edge of the beat than they are at the falling edge. The exact opposite relationship is observable in Figure 6.13(b), which corresponds to the scenario in which the interfering signal is lower in frequency than the reference signal. When filtering out the pulses by means of an optical bandpass filter with a 2 nm bandwidth centered at 1550 nm, different outputs are observed for the two scenarios as a result of the SOA's gain dynamics.

In Fig. 6.13(a) the pulses and peaks at the beat's falling edge are spaced out such that the SOA has adequate time to recover between inputs, and the output pulses are thus amplified to a further extent at these times; however, at the rising edge of the beat, the pulses are temporally closer to the small peaks and thus experience minimal amplification. As such, the output depicted in Fig. 6.13(c) results. When the interfering signal is lower in frequency, however, the output shown in Fig. 6.13(d) occurs due to the now increased spacing between pulses and beat peaks at the beat's rising edge and decreased spacing at the falling edge. The spiking behavior directly relays phase information of the interfering signal. For instance, when the interfering frequency is lower than the reference frequency, the rising edge of the resulting beat always occurs when the interfering sinusoid's positive zero crossings are leading the reference's crossing points, and the falling edge always corresponds to when the interfering sinusoid's crossings lagging behind that of the reference's. The opposite behavior is observed when the interfering frequency is higher than the reference frequency. Consequently, this TS model, which is of the most basic possible design, is reminiscent of the very first LIF photonic neuron [13] and

outputs a “1” when the interfering signal is lagging behind the reference signal and an effective “0” when the interfering signal leads the reference signal.

This model, while successful in conveying the necessary phase information, does not produce the most ideal output. For instance, some of the techniques used by more complete photonic neuron models could be utilized to clean up the TS output. Thresholding by means of a NOLM would suppress the zero level of the signal, which could make for easier signal processing at later stages of the JAR circuit, and an inverter and second thresholder could further serve to increase the disparity between ones and zeros while reversing the logic of the output. The device would then output spikes when the interfering signal leads the reference signal and transmit nothing when the interfering signal lags behind the reference signal.

Figure 6.13. Comparison of TS inputs and outputs for 100 MHz separations between reference and interfering frequencies, with the zero crossing pulses in red and beat signal in blue. (a) TS inputs for a 2.4 GHz reference signal and a 2.5 GHz interfering signal. (b) TS inputs for a 2.4 GHz reference signal and a 2.3 GHz interfering signal. Next, TS outputs are pictured in the two scenarios, showing that the crossing point pulses are amplified the most when the interfering signal is lagging behind the reference signal: (c) Shows when the interfering frequency is greater than the reference frequency by 100 MHz, and (d) shows when the interfering frequency is less than the reference frequency by 100 MHz. Time intervals at which the interfering signal is lagging and leading are indicated by the red text and blue text, respectively.

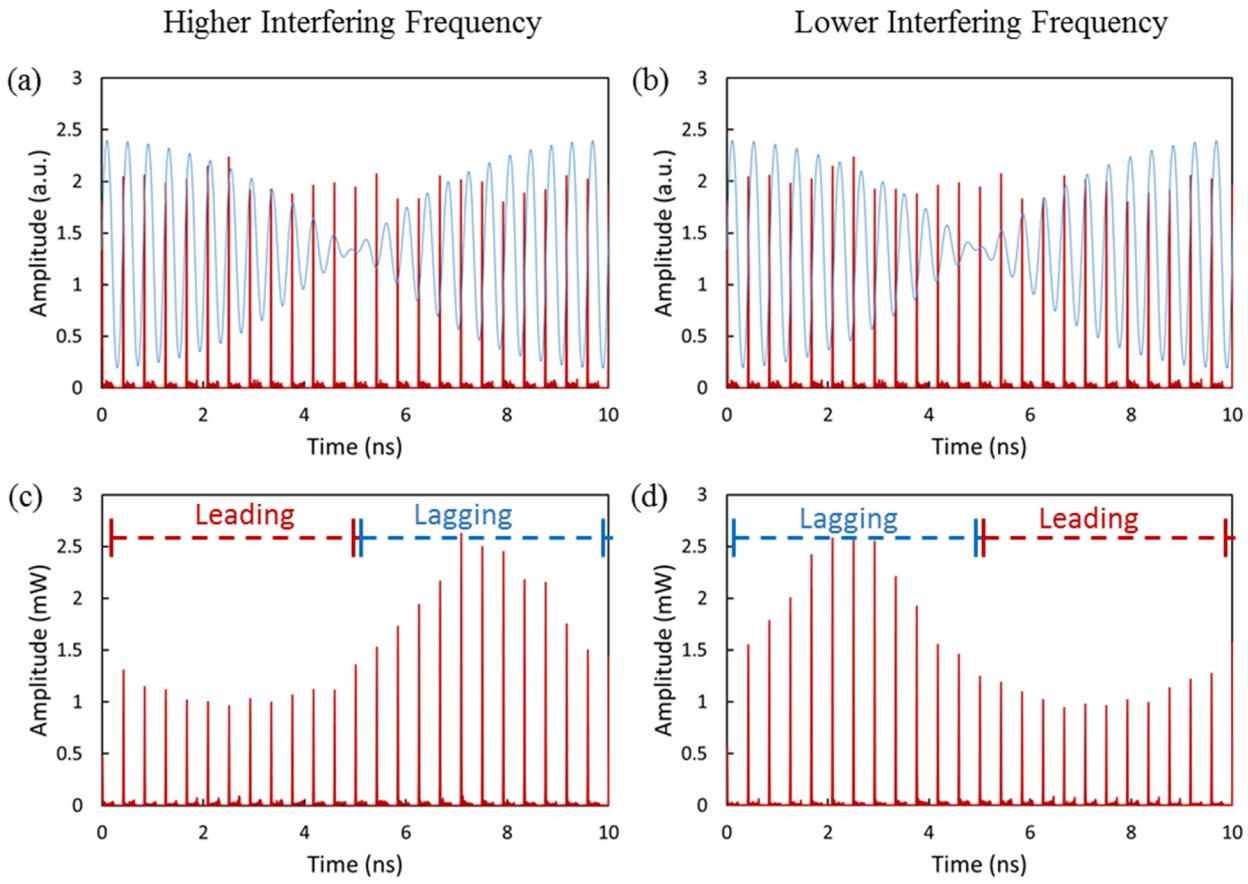

Logic Circuitry and Discussion

The final subsystem of the JAR circuit processes the amplitude and phase information acquired from the P-unit and the TS, making a final decision as to whether or not the transmission frequency is in need of adjustment and in what direction. Operating as a basic XOR or XNOR gate, the decision from the logic circuit can be easily summarized by Table 6.2. For this system, a spike from the P-unit marks the rising edge of the beat envelop, and a spike from the TS indicates times at which the interfering signal is lagging behind the reference signal; however, the logic of the TS can easily be reversed with additional photonic neural components.

Table 6.2. Summary of the JAR logic decision based on amplitude and phase information.

P-Unit (Beat Amplitude Information)	TS (Phase Information)	JAR Decision (Frequency Adjustment)
Increasing (1)	Leading (0)	Increase (1)
Increasing (1)	Lagging (1)	Decrease (0)
Decreasing (0)	Leading (0)	Decrease (0)
Decreasing (0)	Lagging (1)	Increase (1)

This system's inputs are both in the optical domain, and several approaches for XOR or XNOR logic have been proposed and demonstrated that could be applied with this system [60-64]. With beat frequencies in the MHz range, however, optical processing is not essential, and electrical processing is therefore considered for this system. Figure 6.14 shows the inputs for several different interference scenarios after conversion to the electrical domain by photodetectors and passage through 500 MHz low-pass filters. The filtering is implemented because of the different nature of P-unit and TS outputs, with the P-unit transmitting

nanosecond-width pulses at MHz repetition rates, and the TS emitting ultrashort, picosecond-width pulses at GHz repetition rates.

Without adjusting the system parameters for any of the simulation trials, the P-unit and TS exhibit the proper spiking behavior for situations in which the interfering signal is up to 240 MHz higher or lower in frequency than a reference signal at 2.4 GHz; however, in each of the 10 scenarios, minor issues exist. For example, the amplitudes of the TS and P-unit spikes vary by as much as 300 μW, and, while the "zero"-level of the TS output is maintained at around 100 μW for all trials, there exists variance in pulse widths between the logic inputs. Furthermore, particularly at the lower frequencies, the logic inputs do not appear to be temporally aligned, and the pulse shape indicates that FWM is occurring along the falling edge of the beat as well.

By more precisely adjusting the system parameters, several of these issues could be eliminated or at least mitigated. Adding a fixed attenuator to the P-unit or fine tuning of the TS inputs would result in a more even match in amplitude for the logic inputs. Attenuation and amplification of the crossing point pulses and beat signal TS inputs, alongside optimization of the TS's SOA driving current or thresholding and inversion techniques, can significantly alter the TS output. Also, the P-unit output at low frequencies could be minimized by optimizing the driving current to the system's amplifier preceding the HNLF. By uncovering the ideal bias current, the minor leading spike, as seen in Figure 6.9(a) corresponding to the crossing point of the negative envelope with the positive envelope's falling edge, could be minimized if the two HNLF inputs are not of sufficient power to induce FWM. Lastly, the lack of temporal alignment for the lower frequencies is simply a product of simulation, as the software employed has a difficult time accurately representing a wide range of frequencies in a single program.

Figure 6.14. Logic inputs for a 2.4 GHz reference and an interfering signal (a) 25 MHz higher, (b) 25 MHz lower, (c) 50 MHz higher, (d) 50 MHz lower, (e) 100 MHz higher, (f) 100 MHz lower, (g) 200 MHz higher, (h) 200 MHz lower, (i) 240 MHz higher, and (j) 240 MHz lower.

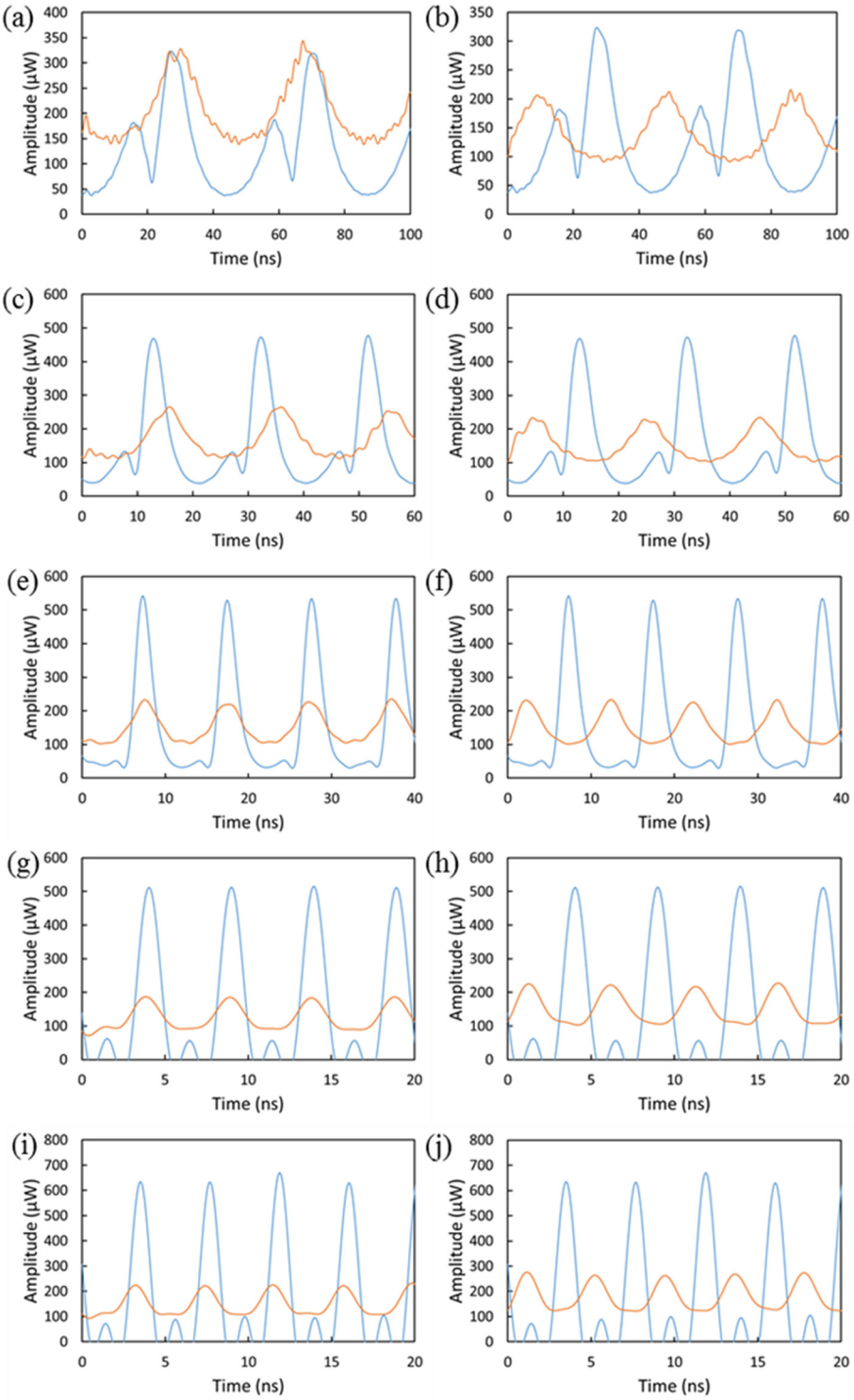

Also, the results describe how a system with a reference signal fixed at 2.4 GHz would respond to different interfering frequencies, when in actuality the reference frequency would be adjusting depending on the logic circuit output. The decision to keep the reference frequency fixed and observe the circuit's response to difference interfering frequencies was made due to further simulation limitations. OptiSystem projects operate on a predefined bit rate, which generation of the NRZ pulses, necessary for positive zero crossing point detection, depends on. If the reference frequency were adjusted from 2.4 GHz by several megahertz, the fixed bit rate of the project would result in an erroneous depiction of the reference signal's crossing points. Despite this shortcoming, the simulations indicate the ability of the system to properly respond to a range of frequency differences, and adjustment of the interfering frequency directly parallels the adjustment of the reference frequency.

Conclusion

The work presented here serves as a proof-of-concept for the most important elements of a photonic JAR circuit, which produce the necessary spiking patterns on which a basic XOR logic gate can operate. For this basic model, a fixed low-pass filter at 250 MHz prevents the P-unit from spiking for frequencies sufficiently far from the reference frequency, providing a potential stopping condition for the JAR circuit. The proposed system does not make use of any strongly frequency-dependent components, allowing for operation over a wide frequency range, with previous simulations successfully operating at frequencies around 10 GHz, and both electrical and optical processing techniques could be implemented in the final decision system [60-64]. Also, all processing techniques used do not depend on the phase of the interfering signal, ensuring that the location of the interfering signal's transmitter is inconsequential to the circuit's outcome. Future iterations of the project will involve complete, autonomous operation

of the JAR circuit, including simulation of NOLM thresholding towards generating the positive zero crossing pulses, envelope detection necessary for rising edge detection of the beat, a XOR/XNOR logic operation on the P-unit and TS outputs, and an adaptive feedback response that properly adjusts and appropriately stops adjusting the reference frequency based on the logic unit's decision. In addition, the system will need to be tested for signals of various modulation formats as only sinusoids at fixed amplitudes are used in the simulations, and a practical system will need to handle a variety of inputs in a realistic environment. Considering the limitations of the OptiSystem software used for this JAR primitive, VPI, a powerful photonic design tool, and MATLAB will be utilized to expand the project. Lastly, individual components of the simulated system will be experimentally verified.

CHAPTER 7

CONCLUSIONS

We have successfully demonstrated a novel photonic STDP circuit based on the cooperative nonlinear effects of XGM and NPR within a single SOA, with the device exhibiting the neuronal learning algorithm on picosecond time scales. Expanding upon the developed system, an AOA-based RF localization scheme capable of centimeter resolution at indoor distances was presented and simulated. This work represents the potential for discovering practical applications in studying the signal processing capabilities of neurobiological systems.

In addition to this, photonic JAR circuitry was developed towards solving spectral scarcity issues in wireless communication networks. The system proved capable of recognizing whether an interfering signal was higher or lower in frequency relative to its own output signal by interpreting amplitude and phase information gained solely from the beating between the two signals. Without any fixed frequency components, the device promises flexibility over a wide frequency range and could be used to probe wireless systems in search of spectral holes for interference-free transmission.

Future works will expand both the localization and JAR projects by means of simulation and experimentation. More advanced, thorough simulations using different software packages will be performed, verifying components previously looked over in the JAR system. Furthermore, a more comprehensive study will test the device's capabilities in working with various modulation formats, and potential issues such as multipath reflection in the localization system will be explored. Lastly, the processing techniques employed in the individual JAR

components will be investigated experimentally. Ultimately, this multipronged work serves to highlight the widespread viability of photonic neuromorphic engineering.

REFERENCES

1. Indiveri, Giacomo, and Timothy K. Horiuchi. "Frontiers in neuromorphic engineering." *Frontiers in neuroscience* 5 (2011).
2. Sarpeshkar, Rahul. "Brain power-borrowing from biology makes for low power computing [bionic ear]." *Spectrum, IEEE* 43.5 (2006): 24-29.
3. Monroe, Don. "Neuromorphic computing gets ready for the (really) big time." *Communications of the ACM* 57.6 (2014): 13-15.
4. Fok, Mable P., et al. "Lightwave Neuromorphic Signal Processing [In The Spotlight]." *IEEE Signal Processing Magazine* 6.27 (2010): 160-158.
5. Froemke, Robert C., and Yang Dan. "Spike-timing-dependent synaptic modification induced by natural spike trains." *Nature* 416.6879 (2002): 433-438.
6. Song, Sen, Kenneth D. Miller, and Larry F. Abbott. "Competitive Hebbian learning through spike-timing-dependent synaptic plasticity." *Nature neuroscience* 3.9 (2000): 919-926.
7. Saleh, Bahaa EA, Malvin Carl Teich, and Bahaa E. Saleh. *Fundamentals of photonics*. Vol. 22. New York: Wiley, 1991.
8. Toole, Ryan, and Mable P. Fok. "Photonic Implementation of a Neuronal Learning Algorithm based on Spike Timing Dependent Plasticity." *Optical Fiber Communication Conference*. Optical Society of America, 2015.

9. Toole, Ryan, and Mable P. Fok. "Photonic implementation of a neuronal algorithm applicable towards angle of arrival detection and localization." *Optics Express* 23.12 (2015): 16133-16141.

10. Tait, Alexander N., et al. "Photonic neuromorphic signal processing and computing." *Nanophotonic Information Physics*. Springer Berlin Heidelberg, 2014. 183-222.

11. Kravtsov, Konstantin S., et al. "Ultrafast all-optical implementation of a leaky integrate-and-fire neuron." *Optics express* 19.3 (2011): 2133-2147.

12. Fok, Mable P., et al. "Pulse lead/lag timing detection for adaptive feedback and control based on optical spike-timing-dependent plasticity." *Optics letters* 38.4 (2013): 419-421.

13. Rosenbluth, David, et al. "A high performance photonic pulse processing device." *Optics express* 17.25 (2009): 22767-22772.

14. Kravtsov, Konstantin, Paul R. Prucnal, and Mikhail M. Bubnov. "Simple nonlinear interferometer-based all-optical thresholder and its applications for optical CDMA." *Optics express* 15.20 (2007): 13114-13122.

15. Melo, A. M., et al. "Time-division multiplexing (OTDM) using soliton pulses in a terahertz optical asymmetric demultiplexer (TOAD)." *Lasers and Electro-Optics, 2001. CLEO'01. Technical Digest. Summaries of papers presented at the Conference on*. IEEE, 2001.

16. Tian, Yue, et al. "Asynchronous spiking neuron based on four-wave mixing and cross absorption modulation." *Optical Fiber Communication Conference*. Optical Society of America, 2012.

17. Fok, Mable P., et al. "Signal feature recognition based on lightwave neuromorphic signal processing." *Optics letters* 36.1 (2011): 19-21.

18. Tait, Alexander N., et al. "Demonstration of WDM weighted addition for principal component analysis." *Optics Express* 23.10 (2015): 12758-12765.

19. Savin, Cristina, Prashant Joshi, and Jochen Triesch. "Independent component analysis in spiking neurons." *PLoS Comput. Biol* 6.4 (2010): e1000757.

20. R. Paschotta, article on 'electroabsorption modulators' in the Encyclopedia of Laser Physics and Technology, 1. edition October 2008, Wiley-VCH, ISBN 978-3-527-40828-3.

21. Gerstner, Wulfram, et al. "A neuronal learning rule for sub-millisecond temporal coding." *Nature* 383 (1996): 76-78.

22. Minai, Ali A., and William B. Levy. "Sequence learning in a single trial." *INNS world congress on neural networks*. Vol. 2. Hillsdale, NJ: Erlbaum, 1993.

23. Abbott, L. F. "Balancing homeostasis and learning in neural circuits." *Zoology*106.4 (2003): 365-371.

24. Blum, Kenneth, and L. F. Abbott. "A model of spatial map formation in the hippocampus of the rat." *Neural Computation* 8.1 (1996): 85-93.

25. Roberts, Patrick D. "Computational consequences of temporally asymmetric learning rules: I. Differential Hebbian learning." *Journal of Computational Neuroscience* 7.3 (1999): 235-246.

26. Mehta, Mayank R., Michael C. Quirk, and Matthew A. Wilson. "Experience-dependent asymmetric shape of hippocampal receptive fields." *Neuron* 25.3 (2000): 707-715. Rao and Sejnowski

27. Hoya, Tetsuya, et al. "Speech extraction based upon a combined subband independent component analysis and neural memory." *Proc. of Fourth Int. Symp. Independent Component Analysis and Blind Signal Separation (ICA2003)*. 2003.

28. Lee, Te-Won, et al. "A unifying information-theoretic framework for independent component analysis." *Computers & Mathematics with Applications* 39.11 (2000): 1-21.

29. Liu, Hui, et al. "Survey of wireless indoor positioning techniques and systems."*Systems, Man, and Cybernetics, Part C: Applications and Reviews, IEEE Transactions on* 37.6 (2007): 1067-1080.

30. Niculescu, Dragos, and Badri Nath. "Ad hoc positioning system (APS) using AOA." *INFOCOM 2003. Twenty-Second Annual Joint Conference of the IEEE Computer and Communications. IEEE Societies*. Vol. 3. IEEE, 2003.

31. Amundson, Isaac, et al. "RF angle of arrival-based node localisation."*International Journal of Sensor Networks* 9.3-4 (2011): 209-224.

32. Gerok, Waldemar, et al. "Influence of the real UWB antennas on the AoA estimation based on the TDoA localization technique." *Antennas and Propagation (MECAP), 2010 IEEE Middle East Conference on*. IEEE, 2010.

33. M. C. O'Connor, "HP kicks off U.S. RFID demo center," http://www.rfidjournal.com/article/articleview/1211/1/50/.

34. Teuber, Andreas, Bernd Eissfeller, and Thomas Pany. "A two-stage fuzzy logic approach for wireless LAN indoor positioning." *Proc. IEEE/ION Position Location Navigat. Symp*. Vol. 4. 2006.

35. Brunato, Mauro, and Roberto Battiti. "Statistical learning theory for location fingerprinting in wireless LANs." *Computer Networks* 47.6 (2005): 825-845.

36. Khan, M. W., Naveed Salman, and A. H. Kemp. "Cooperative positioning using angle of arrival and time of arrival." *Sensor Signal Processing for Defence (SSPD), 2014*. IEEE, 2014.

37. Vo, Nhat, et al. "Weighted nonmetric MDS for sensor localization." *Advanced Technologies for Communications, 2008. ATC 2008. International Conference on*. IEEE, 2008.

38. Zou, Xihua, et al. "Photonic approach to the measurement of time-difference-of-arrival and angle-of-arrival of a microwave signal." *Optics letters* 37.4 (2012): 755-757.

39. Galvanauskas, A., Peter A. Krug, and D. Harter. "Nanosecond-to-picosecond pulse compression with fiber gratings in a compact fiber-based chirped-pulse-amplification system." *Optics letters* 21.14 (1996): 1049-1051.

40. Thomas, Saju, et al. "Programmable fiber-based picosecond optical pulse shaper using time-domain binary phase-only linear filtering." *Optics letters* 34.4 (2009): 545-547.

41. Fu, Libin, et al. "Efficient optical pulse compression using chalcogenide single-mode fibers." *Applied physics letters* 88.8 (2006): 081116.

42. Tait, Alexander N., et al. "The DREAM: an integrated photonic thresholder."*Lightwave Technology, Journal of* 31.8 (2013): 1263-1272.

43. Federal Communications Commission (FCC). Available: http://www.fcc.gov/

44. "Rules for Wireless Broadband Services in the 3650-3700 MHz Band," Federal Communications Commission, 2005. Available: https://apps.fcc.gov/edocs_public/attachmatch/FCC-05-56A1.pdf

45. Buddhikot, Milind M. "Understanding dynamic spectrum access: Models, taxonomy and challenges." *New Frontiers in Dynamic Spectrum Access Networks, 2007. DySPAN 2007. 2nd IEEE International Symposium on*. IEEE, 2007.

46. Niyato, Dusit, Ekram Hossain, and Zhu Han. "Dynamic spectrum access in IEEE 802.22-based cognitive wireless networks: a game theoretic model for competitive spectrum bidding and pricing." *Wireless Communications, IEEE*16.2 (2009): 16-23.

47. Santivanez, C., et al. "Opportunistic spectrum access: Challenges, architecture, protocols." *Proceedings of the 2nd annual international workshop on Wireless internet*. ACM, 2006.

48. Kone, Vinod, et al. "On the feasibility of effective opportunistic spectrum access." *Proceedings of the 10th ACM SIGCOMM conference on Internet measurement*. ACM, 2010.

49. Čabrić, Danijela, et al. "A cognitive radio approach for usage of virtual unlicensed spectrum." *Proc. of 14th IST mobile wireless communications summit*. 2005.

50. Pursley, Michael B. "The role of spread spectrum in packet radio networks."*Proceedings of the IEEE* 75.1 (1987): 116-134.

51. Heiligenberg, Walter. *Neural nets in electric fish*. Cambridge, MA: MIT press, 1991.

52. Lissmann, H. W. "On the function and evolution of electric organs in fish."*Journal of Experimental Biology* 35.1 (1958): 156-191.

53. Lissmann, H. W., and K. E. Machin. "The mechanism of object location in Gymnarchus niloticus and similar fish." *Journal of Experimental Biology* 35.2 (1958): 451-486.

54. Bullock, Theodore H., Robert H. Hamstra Jr, and Henning Scheich. "The jamming avoidance response of high frequency electric fish." *Journal of comparative physiology* 77.1 (1972): 1-22.

55. Laferrière, J., et al. *Reference guide to fiber optic testing*. JDS Uniphase Corporation, 2007. Available: http://www.jdsu.com/ProductLiterature/fiberguide1_bk_fop_tm_ae.pdf

56. LeMoncheck, John E. "An analog VLSI model of the jamming avoidance response in electric fish." *Solid-State Circuits, IEEE Journal of* 27.6 (1992): 874-882.

57. Cha, Jeongwon, et al. "A highly-linear radio-frequency envelope detector for multi-standard operation." *Radio Frequency Integrated Circuits Symposium, 2009. RFIC 2009. IEEE*. IEEE, 2009.

58. Zhou, Yanping, et al. "A novel wide-band envelope detector." *Radio Frequency Integrated Circuits Symposium, 2008. RFIC 2008. IEEE*. IEEE, 2008.

59. Datasheet, LTC5507. "Linear Technology." Available: http://cds.linear.com/docs/en/datasheet/5507f.pdf

60. Jinno, Masahiko, and Takao Matsumoto. "Ultrafast all-optical logic operations in a nonlinear Sagnac interferometer with two control beams." *Optics letters*16.4 (1991): 220-222.

61. Kim, Jae Hun, et al. "All-optical XOR gate using semiconductor optical amplifiers without additional input beam." *Photonics Technology Letters, IEEE*14.10 (2002): 1436-1438.

62. Soto, Horacio, Didier Erasme, and Georg Guekos. "5-Gb/s XOR optical gate based on cross-polarization modulation in semiconductor optical amplifiers."*Photonics Technology Letters, IEEE* 13.4 (2001): 335-337.

63. Yu, Changyuan, et al. "All-optical XOR gate using polarization rotation in single highly nonlinear fiber." *IEEE photonics technology letters* 17.6 (2005): 1232-1234.

64. Fok, Mable P., and Paul R. Prucnal. "All-optical XOR gate with optical feedback using highly Ge-doped nonlinear fiber and a terahertz optical asymmetric demultiplexer." *Applied optics* 50.2 (2011): 237-241.

65. PriTel, Inc. Available: http://www.pritel.com/low_p.htm

66. Premaratne, Malin, Govind P. Agrawal, and Dragan Nesic. "A Systematic Way of Approximating Gain Recovery Dynamics in SOAs." *IEEE Journal of Lightwave Technology* 25.10 (2007): 1.

APPENDIX A

JAR OPTISYSTEM SCREEN CAPTURE

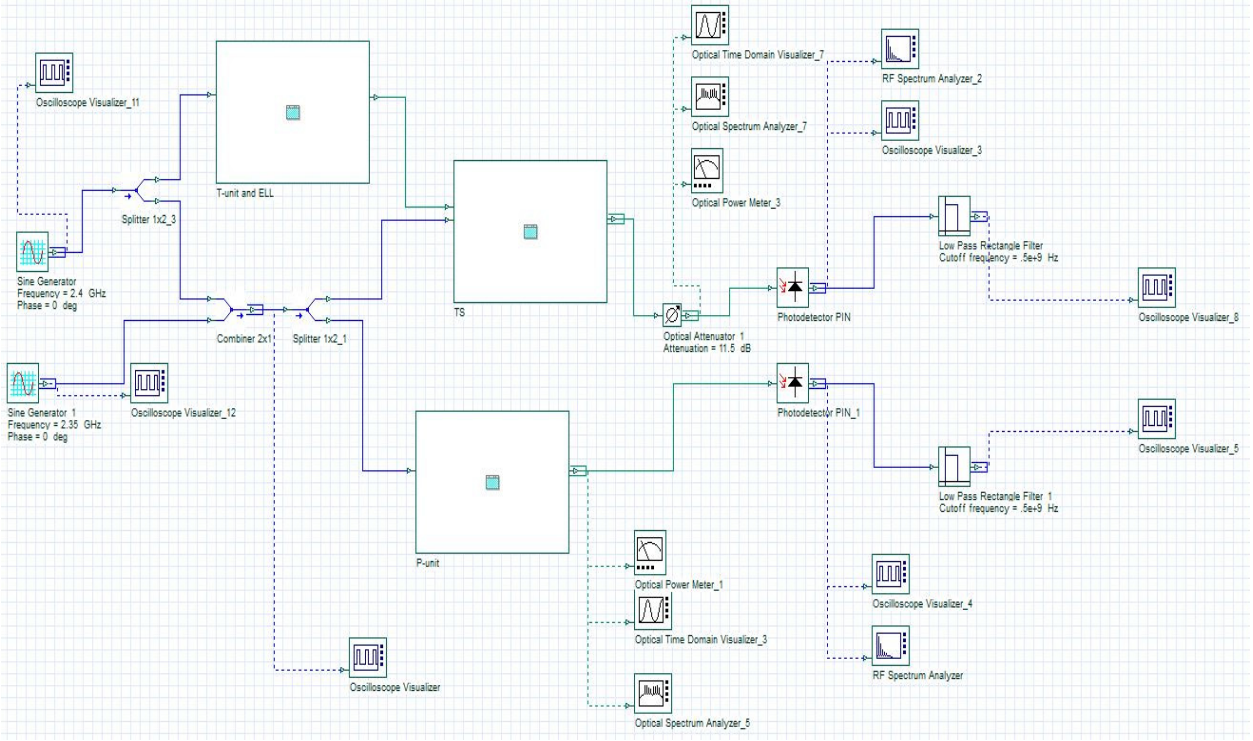

Figure A.1. Screen capture of the complete JAR circuitry as developed in OptiSystem. Here, two signals, the reference and the interference signals, are shown being generated at 2.4 GHz and 2.35 GHz, respectively. The signals are then sent to the three major components of the JAR system, the T-unit and ELL, the P-unit, and the TS unit. The P-unit and TS unit optical outputs are detected by photodetectors, passed through low pass filters, and then observed by oscilloscopes.

APPENDIX B

JAR P-UNIT OPTISYSTEM SCREEN CAPTURE

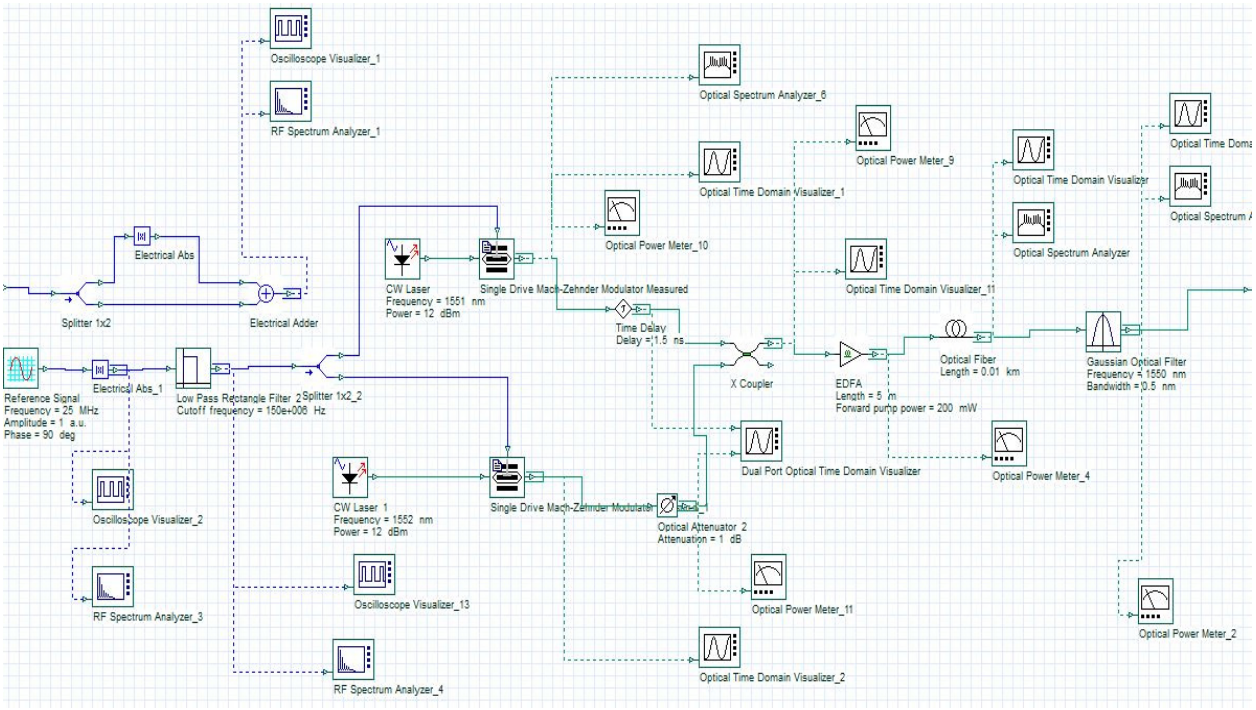

Figure B.1. Screen capture of the P-unit as developed in OptiSystem. Rather than performing envelope detection, a beat of a frequency corresponding to the frequency difference between the reference and interfering signals is directly generated. The beat is then converted to the optical domain by electro-optic modulators (EOMs), producing one upright and another inverted signal. The signals are coupled, amplified and sent through 10 meters of highly nonlinear fiber where four-wave mixing (FWM) occurs. A bandpass filter after the fiber passes a newly generated frequency component, which corresponds to a pulse aligned in time with the rising edge of the original beat signal. Oscilloscopes and power meters are positioned to monitor each step.

APPENDIX C

JAR T-UNIT AND ELL OPTISYSTEM SCREEN CAPTURE

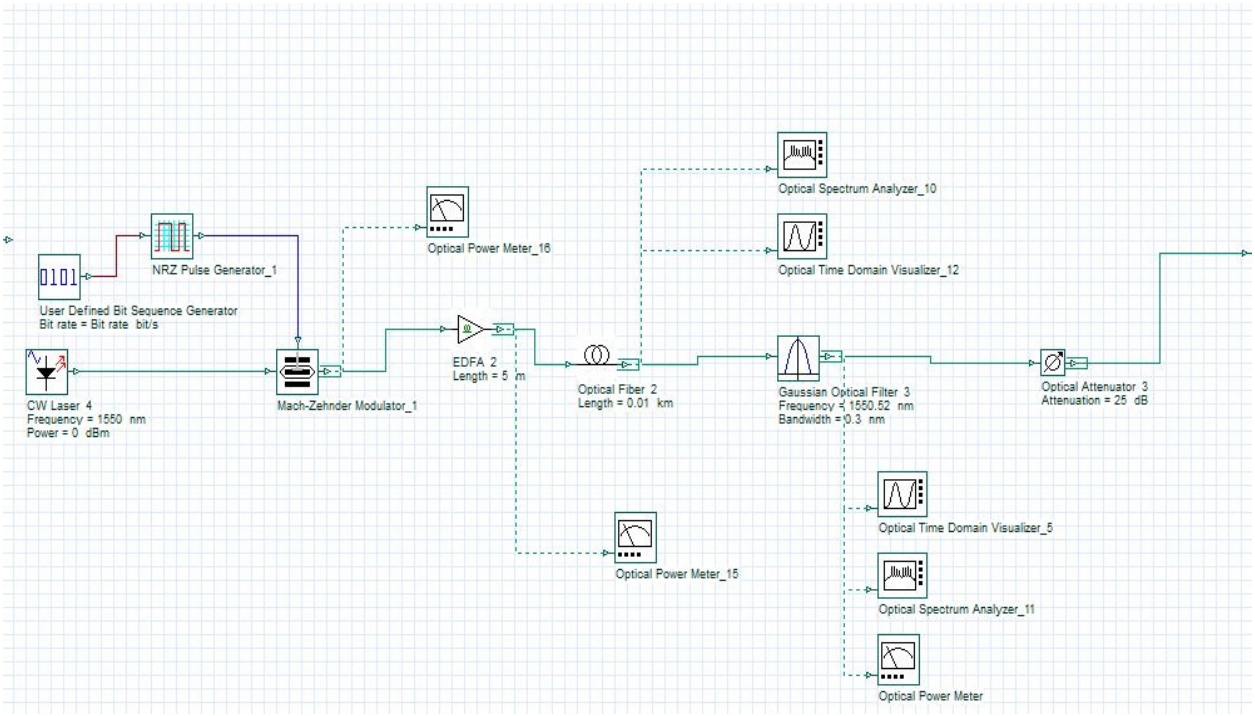

Figure C.1. Screen capture of the T-unit and ELL as developed in OptiSystem. Rather than perform the thresholding to perform amplitude clamping on the 2.4 GHz reference signal, a square-like pulse is generated by a bit sequence generator and a non-return-to-zero (NRZ) pulse generator. The signal is converted to the optical domain by an EOM, amplified by an EDFA, and passed through highly nonlinear fiber in which self-phase modulation (SPM) occurs. The nonlinear optical effect induces a red and blue shift, and the leading edge of the NRZ pulses are passed by a filter centered at the longer wavelength side of the pulse spectrum. Oscilloscopes, power meters, and spectrum analyzers are positioned throughout to monitor the process.

APPENDIX D

JAR TS OPTISYSTEM SCREEN CAPTURE

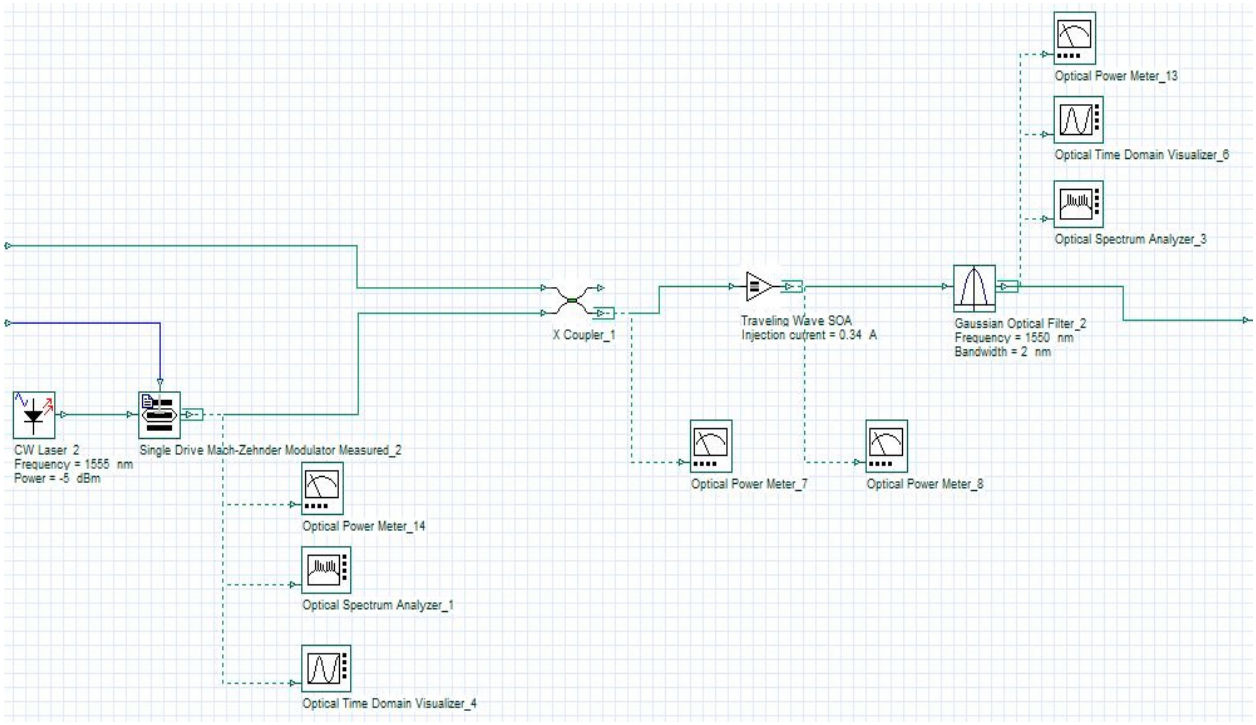

Figure D.1. Screen capture of the TS unit as developed in OptiSystem. The beating signals are converted to the optical domain by an EOM and coupled together with the pulses generated from the T-unit and ELL. The two signals pass through a semiconductor optical amplifier (SOA), and a bandpass filter passes the T-unit and ELL positive zero crossing point pulses, which carry information about the relative phase of the interfering signal.

APPENDIX E

JAR MAJOR COMPONENT PARAMETERS

Table E.1. Parameters used in the simulations. The parameters of the major components responsible for signal amplification, nonlinear effects, and filtering are shown below.

Component	Parameter	Value	Unit	Reference
P-unit Erbium-doped fiber amplifier (EDFA)	Fiber length Pump wavelength Optical gain Optical noise figure	5 980 13 3	m nm dBm dBm	[65]
T-unit EDFA	Fiber length Pump wavelength Optical gain Optical noise figure	5 980 20 3	m nm dBm dBm	[65]
Highly nonlinear fiber (HNLF)	Fiber length Dispersion Nonlinear refractive index	10 -50 2.46×10^{-20}	m ps/nm/km m^2/W	[14]
Semiconductor optical amplifier (SOA)	Driving current Optical gain Confinement factor (Γ) Gain coefficient (a) Carrier recombination coefficient (τ_e)	340 20 0.3 2.78×10^{-20} 300×10^{-12}	mA dBm m^2 s	[66]
Logic circuit electrical bandpass filters	Filter profile Bandwidth	Rectangular 500	 MHz	
P-unit electrical bandpass filter	Filter profile Bandwidth	Rectangular 250	 MHz	
P-unit optical bandpass filter	Filter profile Central wavelength 3-dB bandwidth	Gaussian 1550 0.5	 nm nm	
T-unit and ELL optical bandpass filter	Filter profile Central wavelength 3-dB bandwidth	Gaussian 1550.52 0.3	 nm nm	
TS optical bandpass filter	Filter profile Central wavelength 3-dB bandwidth	Gaussian 1550 2	 nm nm	